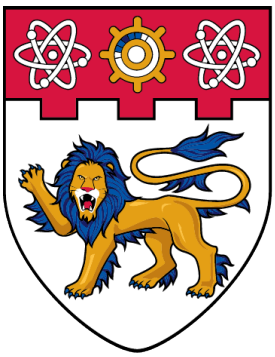

NANYANG TECHNOLOGICAL UNIVERSITY
SINGAPORE

INVESTIGATING GALILEAN INVARIANCE IN CFD

YEO KAI WEN BEVERLEY

SCHOOL OF MECHANICAL
AND AEROSPACE ENGINEERING

2022

INVESTIGATING GALILEAN INVARIANCE IN CFD

YEO KAI WEN BEVERLEY

SCHOOL OF MECHANICAL & AEROSPACE ENGINEERING

A thesis submitted to the Nanyang Technological University
in partial fulfilment of the requirements for the degree of
Master of Engineering (Mechanical & Aerospace Engineering)

Year 2022

Statement of Originality

I hereby certify that the work embodied in this thesis is the result of original research, is free of plagiarised materials, and has not been submitted for a higher degree to any other University or Institution.

08/08/2022

Date

YEO KAI WEN BEVERLEY

Supervisor Declaration Statement

I have reviewed the content and presentation style of this thesis and declare it is free of plagiarism and of sufficient grammatical clarity to be examined. To the best of my knowledge, the research and writing are those of the candidate except as acknowledged in the Author Attribution Statement. I confirm that the investigations were conducted in accord with the ethics policies and integrity standards of Nanyang Technological University and that the research data are presented honestly and without prejudice.

09 Aug 2022

Date

CHAN WAI LEE

Authorship Attribution Statement

This thesis **does not** contain any materials from papers published in peer-reviewed journals or from papers accepted at conferences in which I am listed as an author.

08/08/2022
Date

YEO KAI WEN BEVERLEY

Abstract

When characterizing a body moving in a quiescent flow, like the case of a cruising aircraft, CFD simulations and wind tunnel tests rely on the Galilean invariance principle, which assumes that the moving body can be equivalently modelled by a stationary body with a freestream velocity equal to the motion velocity of the body. However, the validity of this principle for fluid dynamics has not been comprehensively examined before. To this end, this thesis considers numerical simulations of both scenarios and compares the wake and drag coefficient at two Reynolds numbers of 40, where the flow produces a steady wake, and 400, where an unsteady laminar von Kármán vortex street is present. The steady laminar regime represented by the lower Reynolds number shows negligible differences in drag coefficient of the two frames. However, visible differences in the wake of the cylinder were observed. For the unsteady laminar regime represented by the higher Reynolds number, the mean drag coefficient calculated in both reference frames differs by approximately 6%. Additionally, the wake in both frames differs in characteristics and length. Further numerical investigations confirm that these differences are not due to added mass or compressibility effects, thus challenging the assumed invariance of the two reference frames. Future experimental validation is required to prove that the discrepancies are physical and not just numerical artefacts. The Galilean invariance assumption should also be investigated for turbulent flow regimes, for which the change of reference frames could possibly amplify the differences found here due to the large number of timescales involved.

Acknowledgements

This research is supported by the Ministry of Education, Singapore, under its Academic Research Fund Tier 1 (RG141/20). The computational work for this thesis was partially performed on resources of the High-Performance Computing Center, NTU, and National Supercomputing Centre, Singapore (https://www.nscc.sg).

The author also expresses her utmost gratitude to her supervisors, Associate Professor Basman Elhadidi from the School of Engineering & Digital Science, Nazarbayev University, Kazakhstan, and Assistant Professor Chan Wai Lee from the School of Mechanical & Aerospace Engineering, NTU, for the opportunity to work on this extremely interesting and unique CFD project and the many insights throughout the course of the project. In addition, the author is also extremely thankful for their unwavering counsel, support and mentorship provided not just during the course of study when faced with difficulties, but throughout the author's entire time in the university from undergraduate to Masters.

Finally, the author wishes to thank Mr. Melvin Soh from NTU High Performance Computing Center for assistance in running OpenFOAM, and FYP student Mr. Samuel Joo for insights provided through simulating the flat plate case in ANSYS Fluent.

Table of Contents

List of Figures

List of Tables

Nomenclature

Latin symbol

c_d	Coefficient of drag
D	Drag [N]
d	Diameter [m]
Δx	Grid spacing in $x-$axis [m]
Δt	Timestep size [s]
p	Pressure [$\mathrm{kgm^{-1}s^{-2}}$]
q	Dynamic pressure [$\mathrm{kgm^{-1}s^{-2}}$].
Re	Reynolds number
St	Strouhal number
t	Flow time [s]
u_a	Absolute velocity [$\mathrm{ms^{-1}}$]
u_r	Relative velocity [$\mathrm{ms^{-1}}$]
U_∞	Freestream velocity [$\mathrm{ms^{-1}}$]

Greek symbol

ν	Kinematic viscosity [$\mathrm{m^2s^{-1}}$]
ρ	Density [$\mathrm{kgm^{-3}}$]
τ	Non-dimensional flow time
ω	Vorticity [$\mathrm{s^{-1}}$]

Abbreviation

ALE	Arbitrary Lagrangian-Eulerian
CFD	Computational Fluid Dynamics
CFL	Courant-Friedrich-Levy number
DES	Detached-Eddy Simulation
DNS	Direct Numerical Simulation
FFT	Fast Fourier Transform
LBM	Lattice-Boltzmann Method
LES	Large-Eddy Simulation
RANS	Reynolds-Averaged Navier-Stokes
WALE	Wall-Adapting Local Eddy-Viscosity

Chapter 1 Introduction

1.1 Motivation

Computational fluid dynamics (CFD) is commonly used in industrial and academic/research applications as a means to supplement costly and time-consuming experiments. The advancement of computing technology and corresponding increase in computing power available to the modern engineer make simulations of complex flows such as biological flows, flow control, and aircraft propulsion more feasible. Many of these simulations assume Galilean invariance for the benefit of savings in computational cost; this assumption traditionally allows the forces on a body moving in quiescent flow to be modelled equivalently by a statonary body subject to freestream flow. The applicability of this assumption in fluid flows, however, has yet to be thoroughly examined.

The abovementioned assumption may not always hold because, for example, a moving freestream flow over a stationary flow may produce a wake that is convected downstream, whereas, for the same body moving in a stationary fluid, the wake will decay, as shown in Figure 1.1. The assumption needs careful validation particularly for unsteady turbulent flows. Furthermore, for the moving freestream flow, in a simulation, properties of turbulence must be prescribed at the inlet, which may not be an accurate representation of the turbulence generated by the same body moving through a quiescent fluid.

Hence, it will be of interest to investigate the accuracy of such assumptions that are used to solve complex fluid problems. Inaccurate wake structures and behavior especially can lead to inaccurate predictions of aerodynamic properties such as lift and drag, especially in turbulent flows, as the fluctuations induced by unsteady wakes influence the mean pressure distribution over bodies [1].

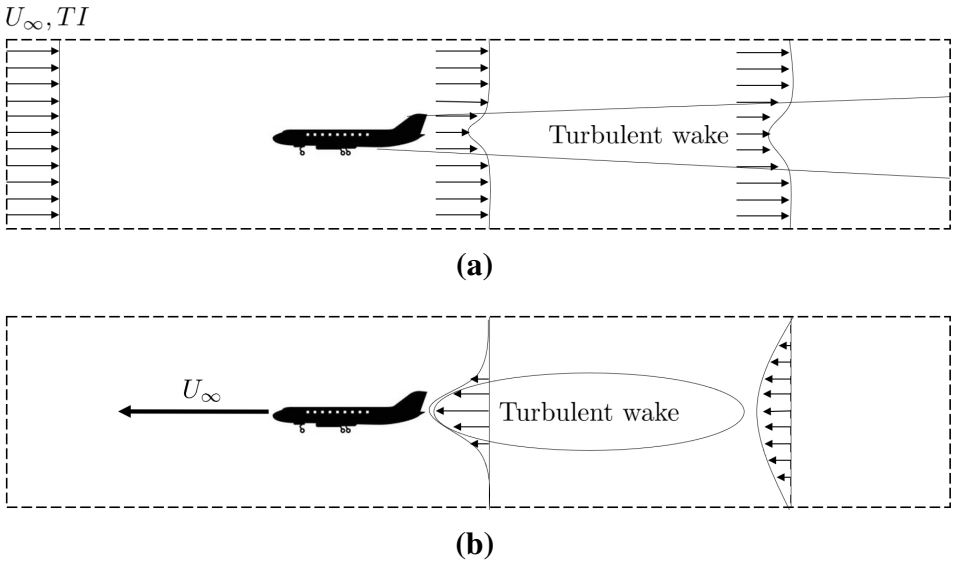

Figure 1.1: Difference in wake between (a) stationary body with incoming freestream flow and turbulence prescribed at inlet and (b) body moving in quiescent flow with turbulence generated by body's motion.

1.2 Background

1.2.1 Galilean Invariance

The principle of Galilean invariance states that the laws of motion do not change in all inertial reference frames [2]. Galilei in 1632 [3] noted that an observer below decks on a ship travelling at a constant speed would not be able to tell whether or not the ship was moving. Engineers have relied on this principle to justify the application of wind tunnel experiments and CFD to determine the forces in a moving frame, for example for aircraft flight testing.

Figure 1.2 shows the the position of a particle in two invariant reference frames, S and S', which are in relative motion with a constant linear velocity $\mathbf{v}$. The position of the point in S is $\mathbf{r}(t) = (x(t), y(t))$ and the position of the same point in S' is $\mathbf{r}'(t) = (x'(t), y'(t))$. The velocities of the point in S and S' are denoted by $\mathbf{u}(t)$ and $\mathbf{u}'(t)$, respectively. Since time is invariant, i.e. $t = t'$,

$$\mathbf{r}'(t) = \mathbf{r}(t) - \mathbf{v}t. \tag{1.1}$$

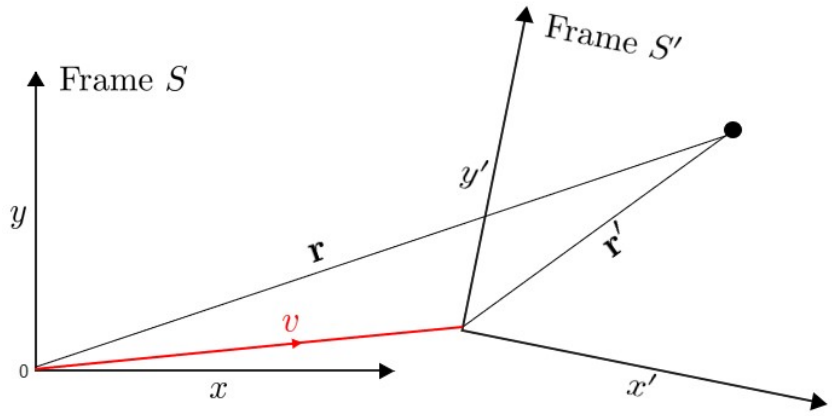

Figure 1.2: Position of a point in two invariant reference frames.

Differentiating Equation (1.1) with respect to time,

$$\mathbf{u}'(t) = \mathbf{u}(t) - \mathbf{v}. \tag{1.2}$$

The acceleration is hence given by,

$$\mathbf{a}'(t) = \frac{d}{dt}(\mathbf{u}(t) - \mathbf{v}). \tag{1.3}$$

Since $d\mathbf{v}/dt = 0$ for a non-accelerating frame,

$$\mathbf{a}'(t) = \mathbf{a}(t). \tag{1.4}$$

Hence, the acceleration in both frames S and S' is the same [4]. Furthermore, since mass of a particle is invariant, force is also frame-invariant as $\mathbf{F} = m\mathbf{a}$. Therefore,

$$\mathbf{F}' = \mathbf{F}. \tag{1.5}$$

In the context of CFD, the Galilean invariance of force has been commonly used to solve the forces acting on objects moving in a stationary, quiescent fluid by calculating the forces in a frame of reference that is fixed to the moving object instead of fixed to the background flow. However, for a fluid, mass and momentum transfer can occur in a control volume and therefore the mass of a fluid parcel may not necessarily be invariant. In addition, Prandtl [5] observes that a change of reference frame also changes the appearance of the wake for a bluff body, as

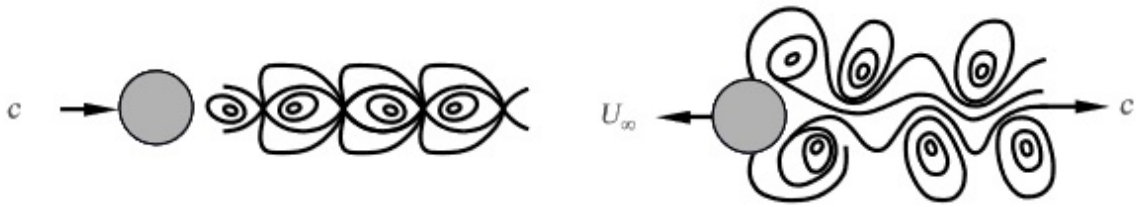

(a) **(b)**

Figure 1.3: Streamlines of von Kármán vortex street observed by (a) observer moving with cylinder and (b) observer fixed in space. Adapted from Ref. [5].

streamlines appear vastly different depending on the observer motion. As illustrated in Figure 1.3, the wakes between the "freestream flow" reference frame with the observer fixed relative to the cylinder (Figure 1.3(a)) and the "moving cylinder" reference frame with the observer fixed in space (Figure 1.3(b)) are clearly visually distinct. However, note that Prandtl used a change of camera position to compare the two reference frames [5], meaning that the cylinder was moving in both figures and the observation in Figure 1.3(a) was made by having the camera moved at the same speed as the cylinder. In the case of a wind tunnel, the observer is fixed in space together with the cylinder and a pressure gradient is present to drive the flow. Hence, the choice of reference frame is important as mass transfer in mixing in wakes across two reference frames is not the same, so the forces can possibly differ across reference frames as well.

Analytical solutions of the Navier-Stokes equations for turbulent flows do not exist except for simple cases. This is despite the fact that most flows in nature are turbulent, characterized by random, stochastic fluctuations of flow properties. Full numerical solutions of the Navier-Stokes equations, also known as Direct Numerical Simulation (DNS) are expensive and costly. Therefore, solution procedures such as the Large-Eddy Simulation (LES), Reynolds-Averaged Navier-Stokes (RANS) or Detached-Eddy Simulation (DES) are often employed in place of a full DNS. Speziale [6] demonstrated (using the concept of force being frame invariant) that the Navier-Stokes equations are Galilean-invariant. Therefore, for a solution to be physical, turbulence must also be described in a Galilean-invariant manner. Hence, turbulence models must be form-invariant for Galilean transformations to be applicable. For example, in LES, the popular Smagorinsky model is Galilean-invariant. However, cross stresses are not, resulting in

Galilean variant equations of motion for the large eddies.

1.2.2 Moving Frames of Reference

Most of the studies regarding simulation of motion of rigid bodies in fluids have been done using the Lattice-Boltzman Model (LBM) or particle-resolved DNS [7–9]. Furthermore, most of the work on Galilean invariance does not target the frame invariance of the simulations but rather addresses the Galilean invariance of turbulence models separately from the mesh or case setups. Lallemand and Luo [7] applied an overset grid combined with the LBM to reduce noise while simulating rigid bodies in two-dimensional (2D) flows. The work focused on developing a scheme that appropriately translates moments between invariant frames. The scheme was tested on a disc moving in a quiescent fluid with both rotational and translational motions at low Reynolds number of 30 and 60. The authors found that the use of overset mesh reduces numerical errors from the cylinder motion by several orders of magnitude compared to traditional non-overset techniques.

Horne and Mahesh [8] developed an unstructured overset method using the arbitrary Lagrangian-Eulerian formulation of the Navier-Stokes equations, which works well with both LES and particle-resolved DNS (PR-DNS). Results suggest that using overset meshing may introduce significant conservation and interpolation errors. However, if implemented appropriately, the overset method can be used to simulate a variety of turbulent flows over geometries of various complexity. Apart from accurately simulating a large number of particles moving in an incompressible stationary fluid, their validation case was within 1% of experimental data and previous LES. Vreman [9, 10] also demonstrated through PR-DNS simulation of the flow around spherical particle(s) in several different configurations that the overset mesh achieved less than 1% error norm, thus outperforming other immersed-boundary methods. These studies demonstrate the usefulness, efficiency and accuracy of overset meshing in moving-body simulations, while suggesting methods to ensure accuracy that can be employed in the present research.

The application of CFD to arbitrarily-moving frames of reference was also studied by Gledhill et al. [11, 12] to calculate forces from flows involving arbitrarily-accelerating missiles. The authors emphasize the need for a consistent Navier-Stokes formulation in between moving frames, but focused heavily on tackling non-linear motion and acceleration terms. It should be noted that if their problem was to be modelled equivalently by a freestream flow over stationary body, the flow would have to arbitrarily accelerate and decelerate via a change of inlet boundary conditions. However, the implementation of moving reference frames was validated using the case of linearly translating airfoil at Mach 0.8, where the coefficient of pressure was similar between the fixed reference frame and the absolute reference frame with the moving airfoil [11]. This indicates that the application of CFD across the reference frames is sound, at least for streamlined bodies such as thin airfoils. Sreedhar and Virmani [13] and Poludnenko and Khokhlov [14] noted that the use of non-inertial frames of reference are likely to result in non-conservative formulation of the Navier-Stokes equations. However, they concluded that this will not likely affect the accuracy of numerical results. Recently, a study [15] also showed that there is negligible difference between stationary and moving frames of reference when calculating drag over a flat plate. However, the flat plate produced different wakes in both reference frames, with a shorter wake length in the stationary case.

While earlier obtained results [16] also observed no difference between the two reference frames in the cases of flat plate and symmetrical NACA airfoil at zero angles of attack, they highlighted large differences for the drag over a cylinder at the Reynolds number of $Re = 400$, ranging from between 14% to 100%. This large discrepancy suggests that Galilean invariance may not apply the same for bluff bodies and/or unsteady flows. Thus, the aim of the current thesis is to further investigate this discrepancy.

1.2.3 Von Kármán Vortex Street

One of the most well-studied phenomena in fluid dynamics is the wake of bluff bodies, most commonly from flow over a cylinder [17, 18]. Cylinder wakes consist of laminar separation bubbles at lower Reynolds numbers of $Re < 100$ and the visually distinctive von Kármán vortex

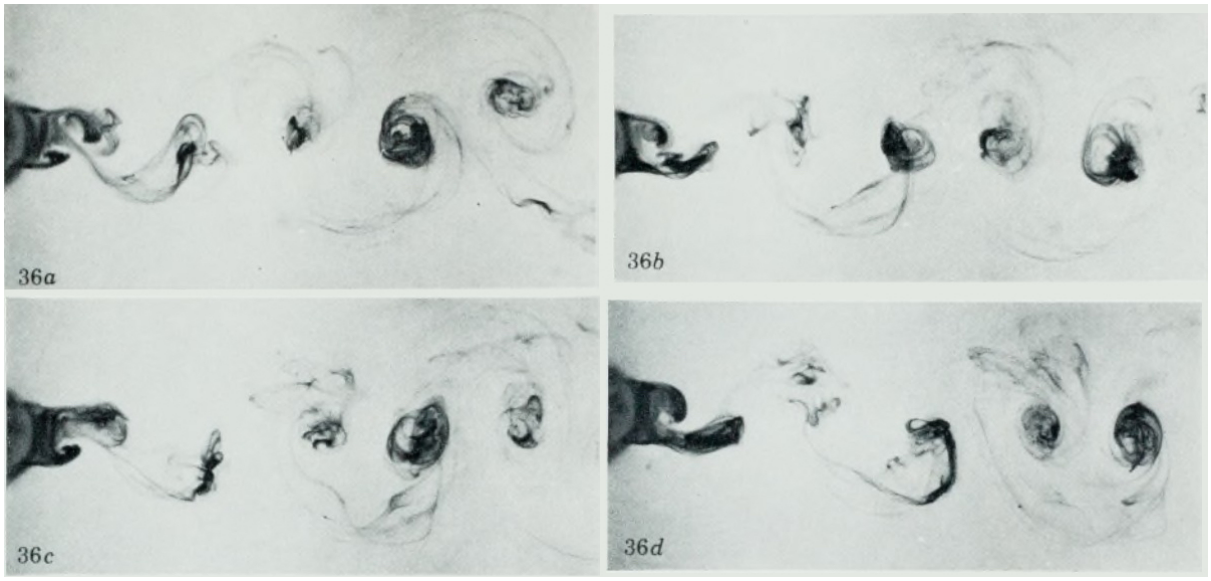

Figure 1.4: Flow visualization of instantaneous cylinder wake at $Re = 407$. Adapted from Ref. [20].

street at moderate and high Reynolds numbers. The plethora of existing literature on this flow phenomena makes it a convenient test case for this thesis. However, as mentioned in Section 1, both computational and experimental studies involving bluff body wakes are conducted with a stationary body placed in a freestream flow to reduce the costs associated with moving a body through a long flume or tunnel. Hence, experiments involving a bluff body moving in a stationary quiescent flow are few.

Gerrard and Lighthill conducted flow visualization for a cylinder translating along a 4m long towing tank [19, 20]. One example of the flow visualization taken for a cylinder moving with $Re \simeq 400$ [20] is illustrated in Figure 1.4, which shows a steady von Kármán vortex shedding. Gerrard and Lighthill also observed that the vortex strength of each shed vortex is irregular and a transition from laminar to turbulent further downstream. Though limited by only instantaneous photographs as no unsteady and time averaged flowfields were measured, Gerrard and Lighthill [20] offered some useful insights regarding the wake behavior of the cylinder. For example, transverse mixing and vortex fingers in the von Kármán vortex street are found to cause the shed vortices to propagate downstream in a straight line parallel to the cylinder.

Coutanceau and Bouard [21, 22] experimentally investigated the wake of impulsively-started

cylinders. While some of the Reynolds numbers evaluated fell within the transitional and turbulent regimes for which von Kármán vortex-shedding would be expected, the flow visualizations only display the laminar separation bubble formed at the start of the flow due to the sudden startup of the cylinder motion.

Papailou and Lykoudis [23] towed circular cylinders through stationary mercury fluid, which is of high density and viscosity, at Reynolds numbers of the order $10^3 - 10^4$. The authors observed that the shed vortices persist far downstream and noted that, at such high Reynolds numbers, the location of the transition to turbulence in the wake depends on the Reynolds number, with transition occuring closer to the cylinder at higher Reynolds numbers. In addition, the authors proposed that the entrainment mechanism of turbulent vortex street differs from that of laminar vortex street. Specifically, the laminar vortex street grows due to viscous diffusion, whereas the turbulent vortex street entrains fluid via turbulent shearing forces.

Taneda [24] observed experimentally that, in addition to the von Kármán vortex street observed in the wakes of bluff bodies, a hydrodynamic instability is present and can cause the street to decay and transform into a secondary vortex street far downstream of the wake. Taneda [24] noted that this secondary vortex street sheds vortices of a larger size at a lower frequency compared to the primary vortex street. Aref [25] observed that the secondary vortices will "pair" with vortices from the primary street during the breakdown. However, the paired vortex street is irregular and short-lived. Later on, Cimbala et al. [26] used smoke-wire visualization to study the downstream development of the cylinder wakes and reaffirmed the conclusions of Taneda [24].

Meanwhile, Inoue and Yamazaki [27] numerically simulated 2D cylinder wakes at Reynolds numbers $Re < 1000$ and observed that the formation of the secondary street is independent of the vortex pair merging. They, along with Dynnikova et al. [28], Kumar and Mittal [29], and Jiang [30], also found that the wake defect increases sharply at the formation/decay region, where a large trough in the centerline velocity profiles of the wakes will therefore be expected. The phenomenon was further investigated by Dynnikova et al. [28] who simulated the towing of a cylinder in a quiescent fluid at different Reynolds numbers ($140 < Re < 1000$). They found

that the primary vortex street decay is attributed to the instability of the vortex street, which will form a dipole cluster that moves upstream together with the bluff body. These observations are useful in visually validating the results of the moving cylinder simulations.

Apart from a cursory description given by Gledhill et al. [11], to the best of the authors knowledge, there have not been studies examining exactly the differences between stationary and moving frames of reference. CFD has been carefully validated by experimental data for stationary bodies in wind tunnels. However, the application of CFD for a moving frame has not been compared systematically with that of a stationary frame.

1.3 Objective & Scope

The objective of this thesis is to compare the wake structure and forces generated by a body moving in a stationary quiescent fluid against that generated from a freestream flow over a stationary body. This comparison will allow a careful examination on the Galilean invariance assumption commonly used for CFD applications.

The scope of work consists of setting up and discretizing the 2D problem in OpenFOAM and investigating 3D effects, CFL number sensitivity, effects of added mass, and effects of compressibility.

1.4 Organization of Report

The rest of this thesis is organized as follows: Chapter 2 details the computational models used and developed for the simulations in this thesis. Chapter 3 discusses the results obtained from the simulations. Chapter 4 describes possibilities for future work and preliminary extensions. The conclusions and future work are given in Chapter 5.

Chapter 2 Numerical Modelling

2.1 Governing Equations

The Arbitrary Lagrangian-Eulerian (ALE) formulation of the incompressible, laminar Navier-Stokes equations, are solved using the open-source code, OpenFOAM. The continuity and momentum equations are given in Equations 2.1 and 2.2 respectively [31]. Note that the rotation terms have been omitted from the formulations as there is no grid rotation to be considered here.

$$\frac{d}{dt}\int \rho dV + \oint \rho \mathbf{n}\cdot(\mathbf{U}-\mathbf{U_g})dS = 0. \tag{2.1}$$

$$\frac{d}{dt}\int \rho \mathbf{U} dV + \oint \mathbf{U}\rho \mathbf{n}\cdot(\mathbf{U}-\mathbf{U_g})dS - \oint \rho \nu \mathbf{n}\cdot\nabla\mathbf{U}dS + \oint p\mathbf{n}dS. \tag{2.2}$$

In the above equations, the mass flux over control surface dS is given by $\phi = \rho\mathbf{n}\cdot(\mathbf{U}-\mathbf{U_g})$. The motion of the overset mesh is handled by the grid velocity, $\mathbf{U_g}$. In the stationary cylinder simulation, the grid velocity is zero, and therefore the above equation reduces to $\phi = \rho\mathbf{n}\cdot\mathbf{U}$, which is the same as for a fixed grid, classical Navier-Stokes formulation. In this manner, both stationary and moving cylinder simulations can be solved robustly using the same consistent formulation of the Navier-Stokes equations despite the different frames of reference used [8].

2.2 Case Setup and Mesh

Most of the simulations were performed in 2D to maintain a more manageable computational cost for the moving cylinder cases. To verify the results of the 2D simulations are valid, some 3D simulations were also performed. Reynolds numbers of 40 and 400, defined according to Equation 2.3, were set with incompressible fluid to represent steady and unsteady laminar flow regimes, respectively. The working fluid is standard air at 288K with a density of $\rho = 1.225$ kg/m^3 and kinematic viscosity of 1.47×10^{-5} kg/ms.

$$Re = U_\infty d/\nu. \tag{2.3}$$

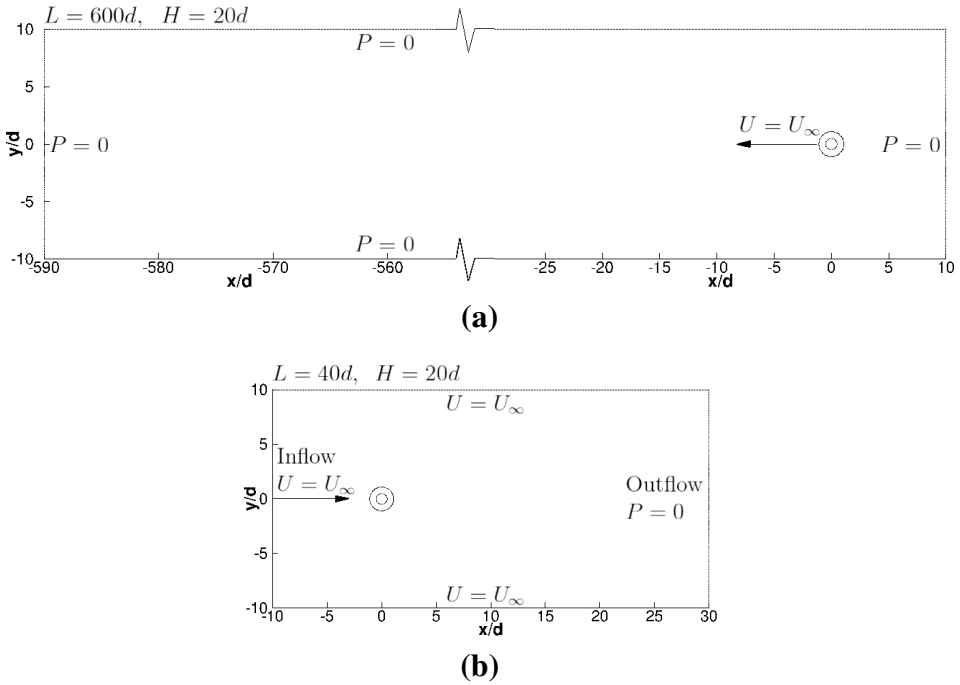

Figure 2.1: Schematic of case setups for (a) moving body in quiescent stationary flow and (b) freestream flow over stationary body.

To represent a bluff body, a circular cylinder was used. The case schematics are illustrated in Figure 2.1, highlighting the dimension and boundary conditions of the moving and stationary body cases and how they are executed.

The meshing strategy is shown in Figure 2.2, where a cylinder-fitted overset mesh refined near the walls was placed in two different background mesh of length $40d$ and $600d$ for the stationary body/freestream flow and moving body/quiescent flow simulations, respectively. Uniform spacing of $\Delta x = 0.05d$ in the $x-$axis and varying spacing in the $y-$axis, refined towards the middle with bias factor 8, were applied on the background mesh of height 20d. For the case of moving body/quiescent flow, the overset mesh translates linearly with a velocity $U = U_\infty$ and all domain boundaries are set as zero pressure (Figure 2.1(a)). Meanwhile, for the case of stationary body/freestream flow, the overset mesh was fixed at $x/d = 0$ and a freestream flow condition with velocity $U = U_\infty$ set at the inlet (Figure 2.1(b)).

The overset patch in Figure 2.2(b) was sized at 3,720 cells with 30 inflation layers using growth rate 1.1 and initial thickness of $0.1\Delta x$. Therefore, the diameter of the overset patch

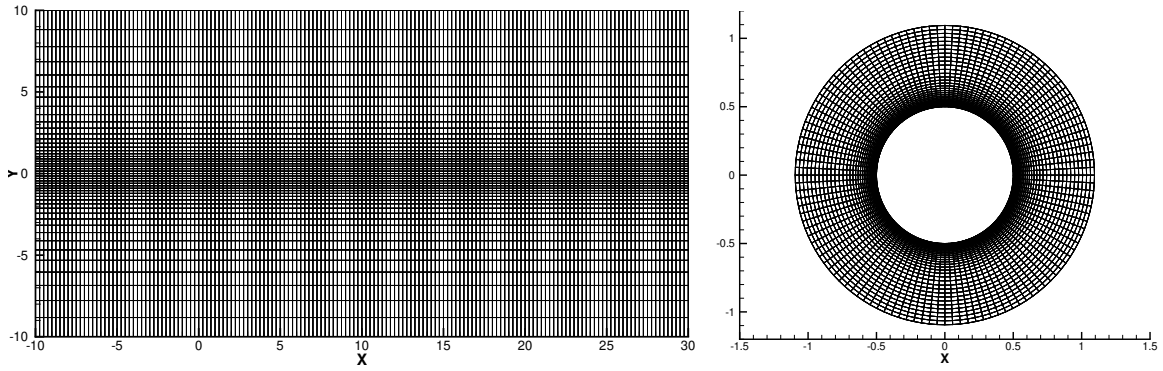

(a) **(b)**

Figure 2.2: (a) Structured background mesh and (b) body-fitted overset grid used in simulation.

is approximately $2d$. This thickness of overset patch was chosen because spurious numerical noise was generated in the moving body simulation when the overset patch is insufficiently thick, likely due to the propagation of inaccuracies caused by data interpolation from the background mesh onto the overset patch. Results from a comparison of overset patch sizing are shown in Appendix A.

2.3 Domain Sizing

The length of the domain in the stationary body simulation is $40d$. For the moving body case, the domain length has to be increased to ensure that the body is able to move far enough for the formation of a steady von Kármán vortex street for the $Re = 400$ simulation. Additionally, the left side boundary, on which a zero pressure boundary condition is imposed, must be far enough from the body such that it accurately represents the farfield atmospheric conditions. Hence, the domain length in this case was increased to $600d$.

The height of the domain was also set such that the farfield is accurately represented. Potential flow theory [32] was used to calculate the height of the potential boundary layer over the cylinder, defined by the position of zero velocity gradient. This happens at approximately $5d$ from the cylinder surface, as illustrated in Figure 2.3. Hence, to account for the possibility of

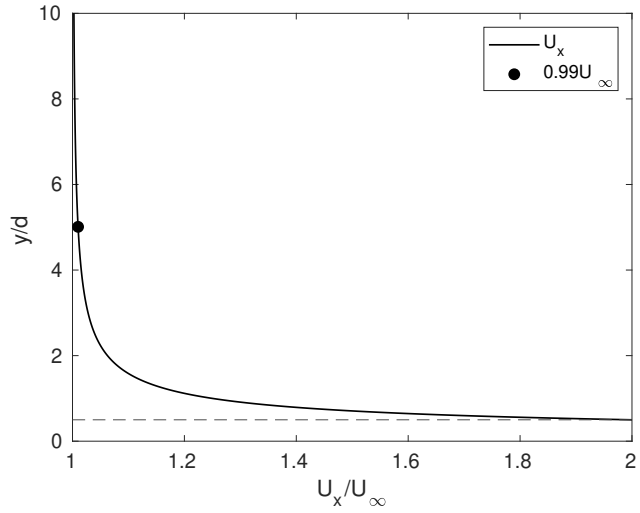

Figure 2.3: Potential layer plot with normalized freestream velocity and height.

the wake widening, the domain's top and bottom boundaries were set at $\pm 10d$, respectively, from the center of the cylinder. Results from the use of different domain size for the moving cylinder case are included in Appendix A.

2.4 Boundary Conditions

The boundary conditions are illustrated in the schematic shown in Figure 2.1.

For the case of freestream flow over stationary cylinder, a velocity inlet with boundary condition $\mathbf{U} = (U_\infty, 0)$ was used on the left of the domain. The top and bottom velocity boundary conditions were also prescribed as $\mathbf{U} = (U_\infty, 0)$ with Neumann boundary conditions for pressure. The velocity was set to the freestream condition as enforcing $\mathbf{U} = \mathbf{0}$ would be equivalent to enforcing a no-slip wall boundary condition, which is inappropriate. As a pressure gradient is required to drive the flow, a zero pressure boundary condition is also inappropriate here. Pressure at the right boundary was set to zero to represent the farfield. The cylinder was fixed in place with a zero velocity Dirichlet boundary condition at the wall.

On the other hand, for the case of the cylinder translating in quiescent flow, all four domain

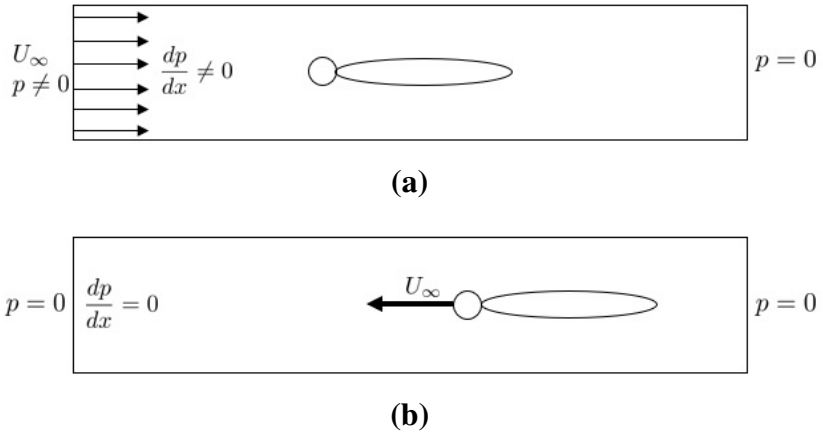

Figure 2.4: Pressure boundary conditions for (a) freestream flow and (b) moving cylinder simulations. The pressure gradient across the domain needs to be non-zero in order to drive the freestream flow but is zero for the moving cylinder.

boundaries were prescribed as Dirichlet boundaries of zero pressure to represent the farfield, while the cylinder wall was set as a moving wall boundary. While both zero pressure and zero velocity boundary conditions would ordinarily be acceptable, $P = 0$ was chosen for the top and bottom boundaries instead so that all four farfield boundaries would use the same boundary conditions. Symmetry boundary condition for the top and bottom of the domain was also examined for the moving cylinder case but found inappropriate (see Appendix B for details).

The boundary conditions and setup represent two real-world scenarios that are often treated as equivalent in engineering, namely: (a) object in motion in a quiescent fluid, for example a ship travelling in still water or a cruising aircraft; (b) the same object fixed in a wind tunnel subject to freestream flow. As such, the boundary conditions are chosen to match these two scenarios.

As shown in Figure 2.4, the stationary cylinder case requires a pressure gradient to drive a freestream flow, which is also done in conventional wind tunnels. Conversely, for the case of the moving cylinder, a pressure gradient is not necessary. While they appear to be equivalent, the two cases in practice may not necessarily represent invariant frames of reference due to the difference in pressure gradient. However, the use of these boundary conditions is justifiable because the aim is to investigate whether these two cases, set up to represent real-world scenarios, will physically result in any differences.

2.5 Selection of CFL Number

To choose an appropriate Courant-Friedrich-Levy (CFL) number, defined by Equation 2.4, and discretization scheme for the convective terms in the Navier-Stokes equation, a simple test was performed by numerically solving the 1D advection-diffusion equation given in Equation 2.5. Upwind and central differencing schemes at different CFL numbers were used to represent the numerical difference schemes used for convection and diffusion terms in most CFD codes.

$$\mathrm{CFL} = \frac{U_\infty \Delta t}{\Delta x}. \tag{2.4}$$

$$u_t + U_\infty u_x = \nu u_{xx}. \tag{2.5}$$

The wavespeed is the freestream velocity U_∞. Upwind differencing for convective terms is combined with central differencing for diffusion terms (Equation 2.6a) and this is compared to a purely central differencing scheme for both convective and diffusion terms (Equation 2.6b).

$$u_i^{n+1} = \begin{cases} \left(\frac{\nu\Delta t}{\Delta x^2} + \frac{a\Delta t}{\Delta x}\right) u_{i-1}^n + \left(1 - \frac{2\nu\Delta t}{\Delta x^2} - \frac{a\Delta t}{\Delta x}\right) u_i^n + \frac{\nu\Delta t}{\Delta x^2} u_{i+1}^n. & \text{(Upwind)} \quad (2.6a) \\ \left(\frac{\nu\Delta t}{\Delta x^2} + \frac{a\Delta t}{2\Delta x}\right) u_{i-1}^n + \left(1 - \frac{2\nu\Delta t}{\Delta x^2}\right) u_i^n + \left(\frac{\nu\Delta t}{\Delta x^2} - \frac{a\Delta t}{2\Delta x}\right) u_{i+1}^n. & \text{(Central)} \quad (2.6b) \end{cases}$$

Von Neumann stability analysis for the above schemes shows that the stability condition for the upwind scheme is given by Equation 2.7a and for the central scheme, Equation 2.7b.

$$\frac{\Delta t}{\Delta x^2}(2\nu - U_\infty \Delta x) < 1. \quad \text{(Upwind)} \tag{2.7a}$$

$$\frac{\nu\Delta t}{\Delta x^2} < \frac{1}{2}. \quad \text{(Central)} \tag{2.7b}$$

Solving Equation 2.5 numerically with an initial condition $u(x,t) = -\sin x$ and periodic boundary conditions, the analytical solution is given by Equation 2.8.

$$u_{\text{analytical}}(x,t) = -\sin(\pi(x - U_\infty t))\exp(-\nu\pi^2 t). \tag{2.8}$$

Results for the upwind scheme show that the error reduces as CFL $\to$ 1, whereas, for the central scheme, the error instead reduces as CFL $\to$ 0. This indicates that the central scheme underpredicts diffusion when the CFL number is too high, while the upwind scheme

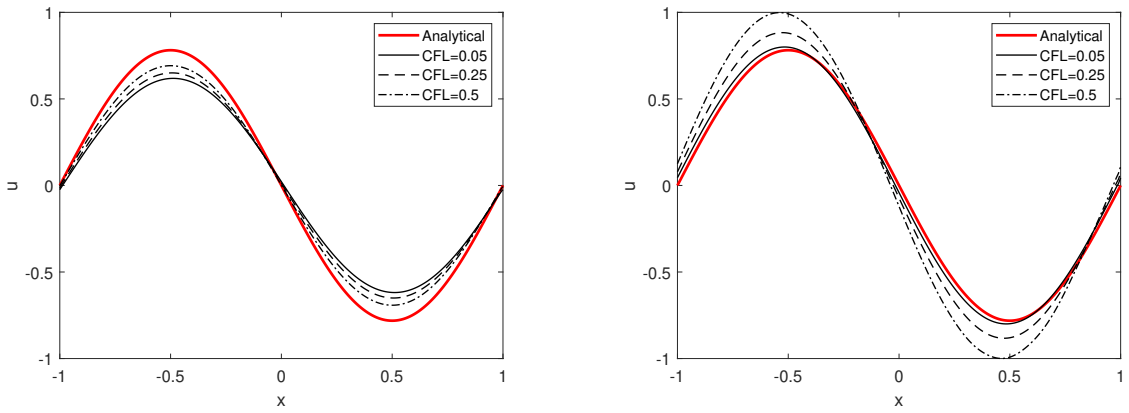

Figure 2.5: Solution of 1D advection-diffusion equation at $t = 10$ s with periodic boundaries and initial condition $u(x,t) = -\sin x$ calculated using (a) upwind and (b) central schemes.

overpredicts diffusion when the CFL number is too low. In literature, this is generally insignificant, as the viscosity term becomes negligible at higher Reynolds numbers ($U_\infty \gg \nu/x$). However, at lower Reynolds numbers, the viscosity has a greater significance as U_∞ and ν/x are of similar orders-of-magnitude. This is illustrated in Figure 2.5, with more added diffusion clearly present in the upwind scheme for lower CFL of 0.05 and less added diffusion for the central scheme at higher CFL of 0.5. This observation can also be derived from the modified equations for the upwind and central schemes, given by Equations 2.9a and 2.9b respectively.

$$u_t + U_\infty u_x = \begin{cases} \left(\nu + \dfrac{U_\infty \Delta x}{2}(1-\text{CFL})\right) u_{xx}. & \text{(Upwind)} \quad (2.9a) \\ \left(\nu - \dfrac{U_\infty \Delta x}{2}\text{CFL}\right) u_{xx}. & \text{(Central)} \quad (2.9b) \end{cases}$$

For stability in accordance with Equation 2.7 the numerical discretization for solving diffusive terms requires CFL < 1. However, as shown in Figure 2.5(a), the upwind scheme produces more accurate results when CFL $\to 1$ and loses accuracy as the CFL number approaches zero. Due to these conflicting requirements from the upwind scheme, the central scheme was chosen for convective terms. The timestep used in the simulations was therefore chosen to be $\Delta t = 0.5$ s, corresponding to an estimated CFL number of 0.06 (based on $\Delta x = 0.05$, $U_\infty = 0.006$ m/s).

2.6 Solver Settings

The simulations were run using the `overPimpleDyMFoam` solver in OpenFOAM v1912, which solves transient incompressible Newtonian flows on a moving overset mesh using the merged PISO-SIMPLE algorithm (PIMPLE) [33]. By default, the `overPimpleDyMFoam` solver uses the arbitrary Lagrangian-Eulerian (ALE) formulation of the Navier-Stokes equations described in Section 2.1 to avoid having different formulations of the equations in different frames of reference [8]. This solver solves each system variable (velocity, pressure, and then turbulence) sequentially, and the overset meshes are coupled via an implicit one-way interpolation [31].

Based on the preceding section and the fact that the central scheme is of a higher Δx^2 order of accuracy compared to the upwind scheme, which is of order Δx, the central scheme was used for convective terms of the Navier-Stokes equations for this study. All other operators, gradient, divergence, and Laplacian, were approximated using second-order central schemes. Linear least-squares approximation was used for interpolation on the overset mesh. A comparison with ANSYS Fluent results are included in Appendix C.

2.7 Post-Processing

2.7.1 Velocity and Vorticity

In all cases presented in Chapter 3, the velocity contours and profiles shown are for the relative velocity for the case of the moving cylinder where the motion velocity U_∞ was added to the flow such that $\mathbf{u_r} = \mathbf{u} + U_\infty \mathbf{i}$. In the freestream flow case, the absolute velocity was plotted instead. Additionally the vorticity for unsteady flow as given by Equation 2.10 was also calculated from the relative velocity for the moving cylinder case and the absolute velocity for the freestream flow case.

$$\omega = \nabla \times \mathbf{u}. \tag{2.10}$$

2.7.2 Forces

Force on the cylinder was calculated by summing up the normal pressure forces and tangential viscous forces over all cells on the cylinder surface in accordance with Equation 2.11. The force vector $\mathbf{F}(t) = (D(t), L(t))$ was then decomposed into drag and lift, respectively, the component of forces in the $x-$ and $y-$axis. In Equation 2.11, $\mathbf{s}_{f,i}$ refers to the face area vector of the cell and $\mathbf{R}_{dev}$ is the deviatoric stress tensor.

$$\mathbf{F} = \sum_i \left(\rho_i \mathbf{s}_{f,i} p_i + s_{f,i} \cdot (\rho \nu \mathbf{R}_{dev}) \right). \tag{2.11}$$

The calculated drag was then time-averaged and normalized by Equation 2.12, where T refers to the averaging time period.

$$\overline{c_d} = \frac{\frac{1}{T}\int_0^T D(t)dt}{0.5\rho U_\infty^2 d}. \tag{2.12}$$

A Fast-Fourier Transform (FFT) was performed on the calculated lift, $L(t)$, to determine the vortex-shedding frequency, f, from which the Strouhal number is calculated according to Equation 2.13.

$$St = fd/U_\infty. \tag{2.13}$$

Performing FFT on the lift is preferred over the drag as the amplitude of the oscillating lift is higher, thus improving the signal-to-noise ratio and highlighting the highest peak frequency (i.e., the vortex-shedding frequency).

2.7.3 Time-Averaging

To fairly compare the wake of the stationary body in freestream flow with the wake of the same body moving in a quiescent fluid, two types of flowfield averaging were carried out. First, the wakes were time-averaged over a body-fixed window, as shown in Figure 2.6(a), which, in the case of the moving cylinder, translates together with it. For the stationary cylinder, the window does not move. Additionally, to translate the problem to the stationary reference frame, the motion velocity U_∞ was added to the calculated velocity of the moving cylinder case, such that

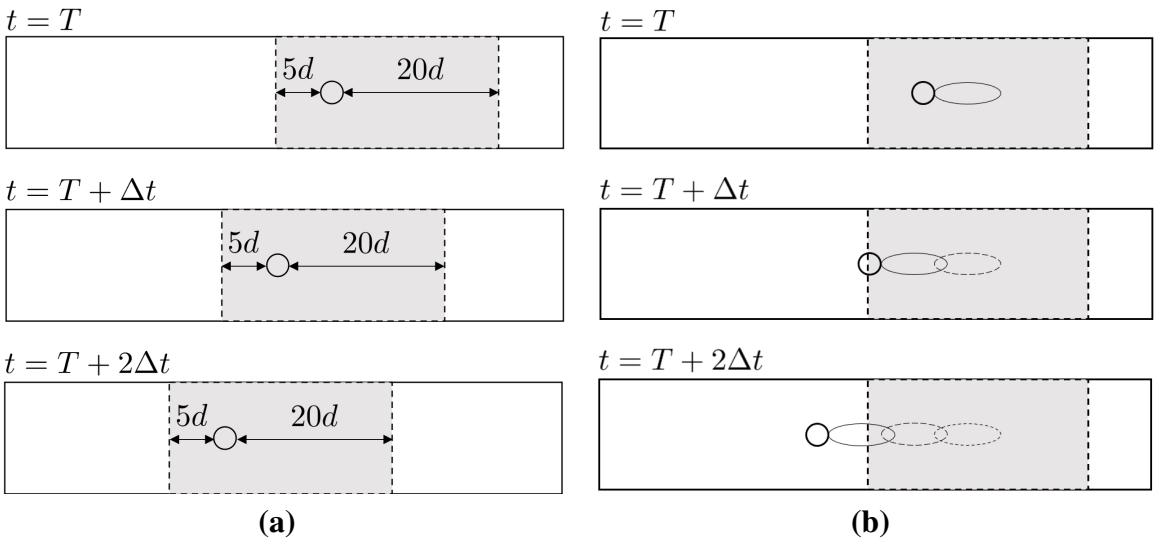

Figure 2.6: Schematic of (a) spatially-moving cylinder-fixed window and (b) background-fixed window for averaging of moving cylinder flow.

$\mathbf{u_r} = \mathbf{u} + U_\infty \mathbf{i}$ is presented instead. This approach allows the near-field behavior of the wake to be captured. The averaging was started after the flow has reached the steady or quasi-steady state and calculated according to Equation 2.14, where i is the spatial index and j is the temporal index of the data point.

$$\overline{\mathbf{w}_i} = \left[\frac{1}{N} \sum_{j}^{N} \mathbf{w}(\mathbf{x}_i, t_j) \right]_{t=T_0}^{T_0+T}. \tag{2.14}$$

For the case of the freestream flow, $\mathbf{w} = \mathbf{u}$ in Equation 2.14. For the case of the moving cylinder, $\mathbf{w} = \mathbf{u_r}$. Also, in the case of the $Re = 400$ cylinders, the quasi-steady state was taken to be the time when the vortex dipole pair observed by Dynnikova [28] began translating at a constant velocity relative to the cylinder. The averaging captured about two vortex-shedding periods for each case, which is sufficient to capture the behavior of the wake since the flow is quasi-steady.

The wakes were also probed over a background-fixed window as shown in Figure 2.6(b), which the moving cylinder translates away from. In the freestream flow simulation, the probe volume will therefore translate downstream from the cylinder. This analysis allows the same patch of vorticity or turbulence generated by the cylinder to be observed over a period of time, and is useful in examining the farfield response of the wake. For this averaging procedure,

quantities were spatially-averaged over a fixed volume instantaneously for every timestep t_j, using Equation 2.15.

$$\overline{\mathbf{w}_j} = \frac{1}{N}\sum_{i}^{N}\mathbf{w}(\mathbf{x}_i, t_j). \tag{2.15}$$

Here, the problem was translated into the background-fixed reference frame by removing the freestream velocity such that $\mathbf{u_a} = \mathbf{u} - U_\infty \mathbf{i}$. Hence, in Equation 2.15, $\mathbf{w} = \mathbf{u_a}$ for the freestream flow simulation, while $\mathbf{w} = \mathbf{u}$ for the case of the moving cylinder.

2.8 Computing Requirements

Resources of the High-Performance Computing Center, NTU, were used to run the simulations. The stationary cylinder simulations were run on a single node with 32 Intel Skylake Xeon(R) Gold 6142 cores and 384GB RAM, while the moving cylinder simulations were run on a different single node with 128 AMD EPYC 7702 cores and 1TB RAM. Additionally, it was found that the `overPimpleDyMFoam` solver in OpenFOAM v1912 scales very linearly up to 600 cores, with the time per iteration halving every time core count was doubled.

Pre- and post-processing was done on a home workstation with a 6-core AMD Ryzen 5 3600 processor and 32 GB of DDR4 RAM. For pre-processing, the background mesh was generated using the built-in `blockMesh` utility in OpenFOAM v1912, while the overset mesh was generated using Pointwise V18.3. Meanwhile, for post-processing and data visualization, a combination of built-in OpenFOAM tools and TECPLOT 360 were used.

Chapter 3 Results & Discussion

3.1 Grid Independence

To ensure grid independence, the mesh illustrated in Figure 2.2 was refined by a factor of two in both the $x-$ and $y-$axes for the $Re = 400$ simulation, twice. This was done holding the CFL number constant at CFL=0.06.

Table 3.1 summarizes the changes in the mean drag coefficient, $\overline{c_d}$, and Strouhal number, St, for the stationary cylinder simulation with the grid refinements. The minimal changes in Table 3.1 indicate that the mesh in Figure 2.2 is sufficient to resolve the flow. Additionally, the Kolmogorov microscale at $Re = 400$ was found to be of order 10^{-2}, the same order of magnitude as the grid spacing used. Since the Kolmogorov microscale increases for smaller Reynolds number, at $Re = 40$, the same grid used would be sufficient to resolve the flow.

For the moving body simulation, the grid independence check was done by refining the mesh selectively in the region $x \in [-200,0]$ with the remaining domain using the coarsest $\Delta x = 0.05$ cell spacing. This is to reduce the computational cost associated with the grid independence check. The results in Table 3.2 indicate that the original grid is sufficient in resolving the flow for the translating cylinder simulation. It should be noted that four-times grid refinement was not done for this simulation due to the high computational cost required.

Table 3.1: Summary of drag coefficients and Strouhal number for stationary cylinder grids

Cell count	Mean c_d	%difference	St	%difference
195,720	1.4444	3.3338	0.2083	0.0000
782,880	1.4180	1.4451	0.2083	0.0000
3,131,520	1.3978	-	0.2083	-

Table 3.2: Summary of drag coefficients and Strouhal number for moving cylinder grids

Cell count	Mean c_d	%difference	St	%difference
2,883,720	1.3667	-1.7964	0.2083	0.0000
5,784,880	1.3917	-	0.2083	-

3.2 Validation

Tables 3.3 and 3.4 summarize, for $Re = 40$ and $Re = 400$ respectively, the mean drag coefficient and Strouhal number obtained from the stationary cylinder simulation of the present work and from previous literature. The minimal differences in the current results compared to both previous computational and experimental work indicate that the results are accurate and reliable. For the lower Reynolds number of $Re = 40$, vortex-shedding is not expected nor observed, so the Strouhal number is inapplicable. The maximum discrepancy of 5.46% between the current result and the measurements of Triton [34] is also observed for other simulations at this Reynolds number [35–39] that were considered. For the higher Reynolds number of $Re = 400$, both the mean drag coefficient and the Strouhal number compare well with the previous studies, with the only significant difference being an 11% change in the Strouhal number between the current study and the simulations of Rajani et al. [40]. However, the current Strouhal number result compares well with the experimental results, notably that of Wen et al. [41].

Additionally, the calculated wake from the moving body simulation, shown in Figure 3.1(a), also closely resembles that calculated by Dynnikova et al. [28] in the range $Re < 600$, as shown in Figure 3.1(b), with the vortex dipole pair clearly visible at around $x/d \approx 30$ downstream of the cylinder. Visual resemblance between the cylinder at $Re = 400$ and the cylinders translating

Table 3.3: Tabulated values of mean drag coefficient, $\overline{c_d}$, for $Re = 40$.

Type	c_d
2D CFD [35–39]	1.51 - 1.67
3D Experiment [34]	1.48
Present work (2D CFD)	**1.52 - 1.56**

Table 3.4: Tabulated values of mean drag coefficient, $\overline{c_d}$ and Strouhal number, St, for $Re = 400$.

Type	$\overline{c_d}$	St
2D CFD [39, 40]	1.39 - 1.42	0.235
2D Experiment [41, 42]	1.40	0.205 - 0.215
3D Experiment [43, 44]	-	0.203 - 0.205
Present work (2D CFD)	**1.37 - 1.45**	**0.210 - 0.217**

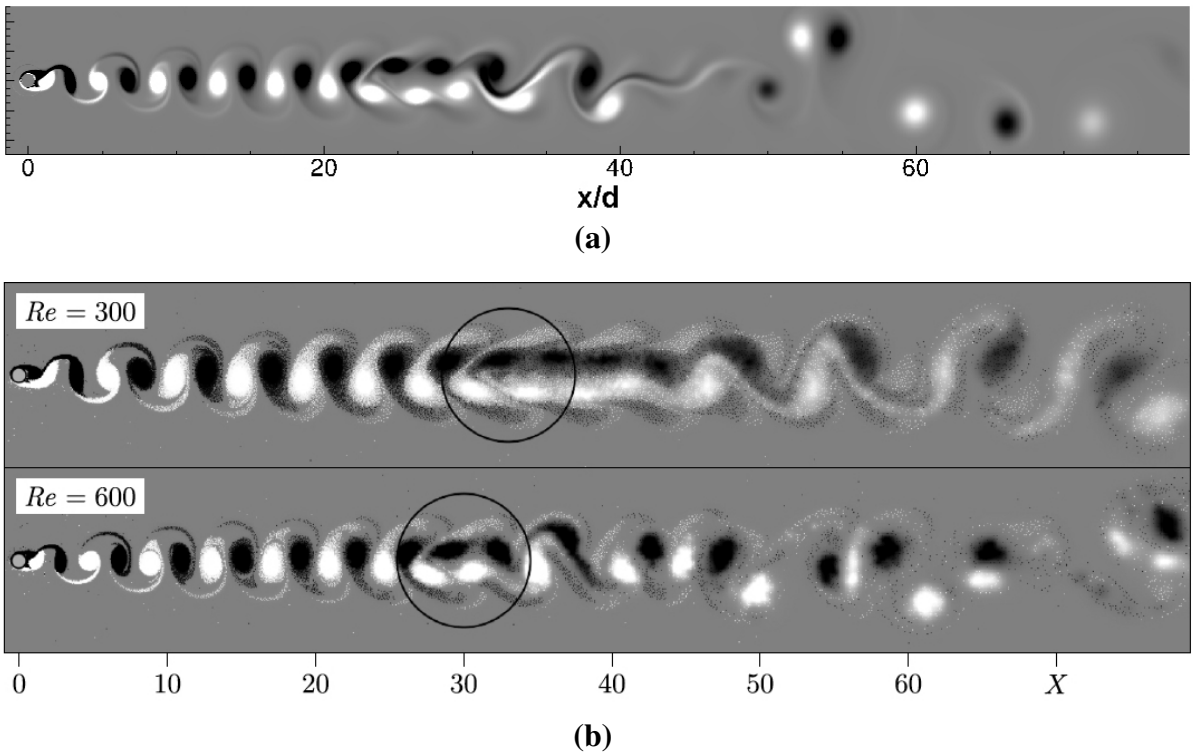

Figure 3.1: Visual comparison of translating cylinder wake between (a) current simulation at $Re = 400$ and (b) Dynnikova et al. [28].

along at $Re = 300$ and $Re = 600$ can be seen clearly from Figure 3.1. Downstream of the dipole pair, the secondary vortex street is in the process of being formed. Though secondary vortex streets are extremely variable and difficult to quantify or compare [28], similarity in the primary vortex street before the dipole cluster suggests that the current simulations are physically correct.

3.3 Steady Flow

The steady laminar regime is represented by the result at $Re = 40$. For this Reynolds number, the stationary body in freestream flow and moving body in quiescient flow display the same flow characteristics and flow behavior, with a calculated steady drag coefficient of $c_d = 1.56$ for the freestream flow and $c_d = 1.53$ for the moving body. With a less than 2% difference calculated in the drag coefficients, the two frames of reference are effectively identical in terms of forces.

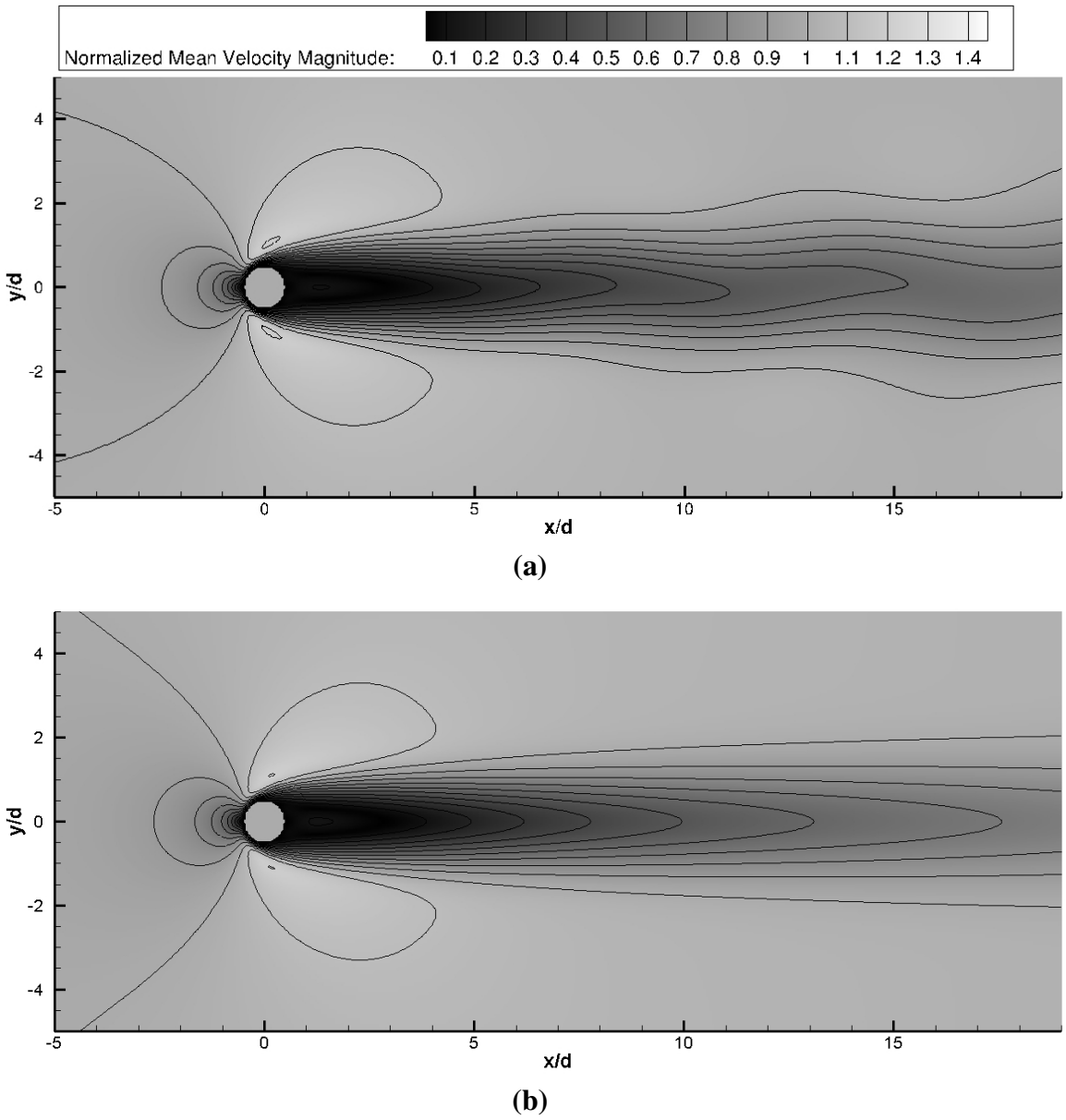

Figure 3.2: Comparison of time-averaged velocity for $Re = 40$ between (a) freestream flow and (b) moving body at quasi-steady flow time $\tau = 12$.

However, the calculated wake for the freestream flow, as shown in Figure 3.2(a), results in some waviness downstream, which is not observed in the moving body case in Figure 3.2(b). Note that the relative velocity $\mathbf{u_r} = \mathbf{u} + U_\infty \mathbf{i}$ is plotted for the moving body simulation so that comparison with the freestream simulation can be made. Visually, the upstream velocity contour of the two cases is also slightly different.

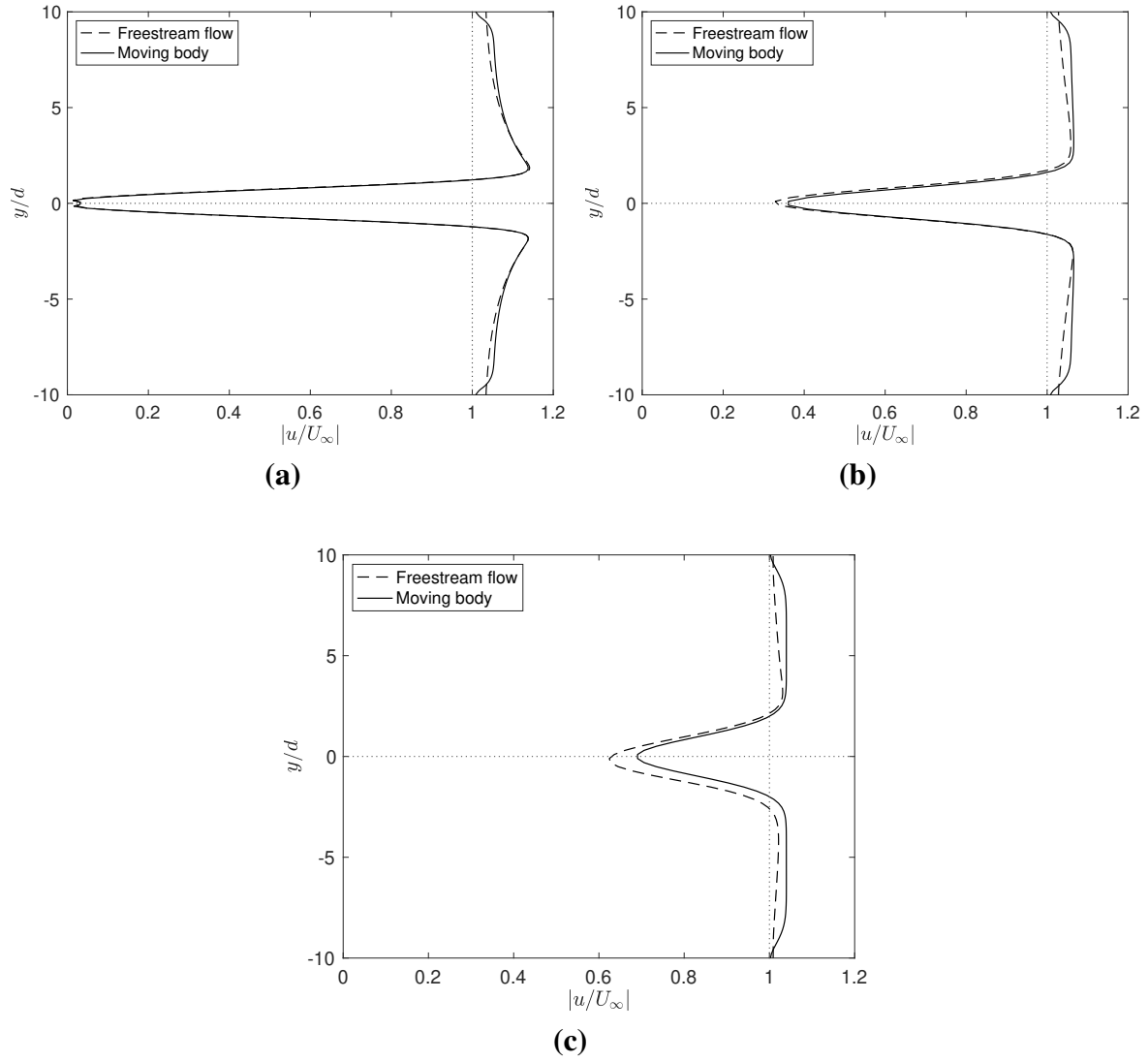

Figure 3.3: Velocity profiles at distances (a) $2d$, (b) $7d$ and (c) $17d$ downstream relative to cylinder at $Re = 40$.

Figure 3.3 shows the relative velocity profiles of the wake for $Re = 40$ taken at $2d$, $7d$, and $17d$ downstream of the cylinder in the body-fixed window. The figures show that, while the behavior of the near-wake is similar across both reference frames, the velocity profiles diverge far downstream at $17d$ from the cylinder. In particular, the moving cylinder's wake deficit recovers faster than the stationary one. Furthermore, in the vertical farfield at $y = \pm 10d$, both wakes behave differently: The velocity in the freestream flow gradually returns to freestream condition, while that in the moving case seems to return to the atmospheric condition with a

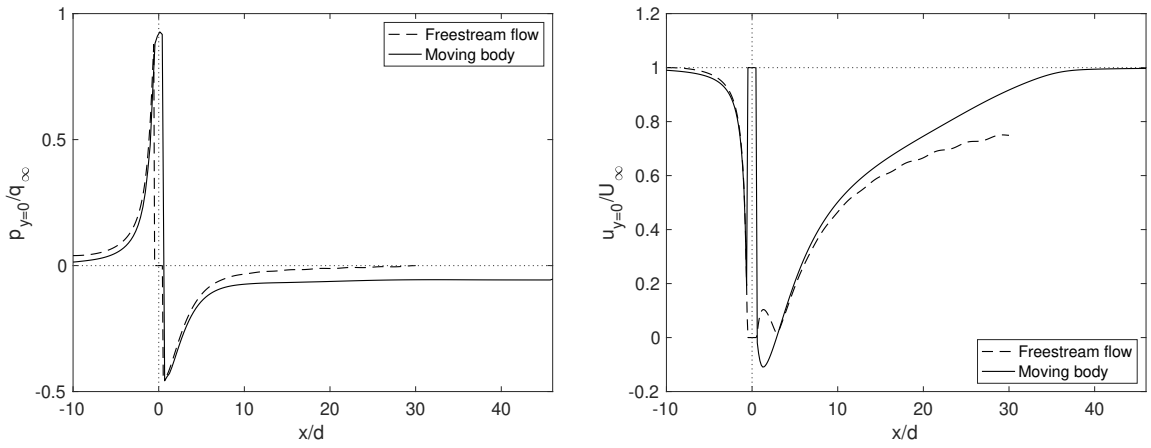

(a) **(b)**

Figure 3.4: Comparison of (a) centerline pressure and (b) centerline velocity across domain length for $Re = 40$.

sharp gradient near the edge.

Figure 3.4(a) compares the centerline pressure in the stationary frame with the centerline pressure in the moving frame, where some differences are visible between both reference frames. The freestream flow appears to quickly return to the zero pressure condition at the outlet. In contrast, the moving cylinder does not reach the zero pressure boundary condition even far downstream at $x/d > 40$. This discrepancy is attributed to the low Reynolds number that results in the $\nabla \mathbf{u}/Re$ term being significant and hence the solver using the central scheme may not be able to impose zero pressure without instabilities being introduced. Note also that the simulation of the freestream flow calculates a higher inlet pressure than the moving body simulation. Figure 3.4(b) makes the same comparison for time-averaged centerline velocity. Contrary to the centerline pressure, the centerline velocity of the moving body returns to the freestream conditions downstream. For the freestream flow, the wake deficit fails to recover, similar to the observation seen in Figure 3.3.

3.4 Unsteady Flow

The unsteady laminar regime is represented by the result at $Re = 400$, for which a quasi-steady von Kármán vortex street is expected to form behind the cylinder, starting with a primary vortex street, followed by a secondary vortex street after the decay of the primary street [24, 28]. Hence, the time-averaging strategies described in Chapter 2 were started only after the vortex street has reached a quasi-steady state with the vortex-dipole cluster described by Dynnikova et al. [28] remaining at a constant distance behind the cylinder.

For this Reynolds number, the coefficients of drag calculated were $\overline{c_d} = 1.44$ for the freestream flow and $\overline{c_d} = 1.37$ for the moving cylinder, with corresponding Strouhal number of $St = 0.2083$ for both simulations. Therefore, there was no difference in the calculated Strouhal number, and the difference in drag coefficient was 5.69%.

Figures 3.5 and 3.6 present the instantaneous vorticity contour plot and time-averaged velocity field in the body-fixed window for the cylinders at $Re = 400$. Figure 3.5(a) shows that in the farfield at $x/d \approx 25$ the vortices in the freestream flow case begin to show decreasing core-to-core separation. This is not seen in the moving case, as shown in Figure 3.5(b), for which the vortex street is steady and laminar at that distance. Additionally, the vortices in the farfield $x/d > 15$ for the freestream flow case are increasing in size, which indicates the beginning of the transition into the secondary vortex street caused by hydrodynamic instability [26]. This is not seen for the moving body simulation where the transition seems to occur further downstream. In fact, the time-averaged velocity field shows that the wake is narrowing downstream in the moving body case. Visually, the plots in Figure 3.6 are comparable to those in Dynnikova et al. [28] and Jiang [30] where a larger wake deficit is observed in the downstream region.

Like Figure 3.4, Figure 3.7 also displays only a cropped $40d$ window for the moving body simulation's domain, so the moving body simulation is not expected to have returned to the zero pressure boundary condition in Figure 3.7(a). Conversely, the centerline pressure of the freestream flow scenario returns to atmospheric condition at the domain boundary. These results are similar to the steady flow $Re = 40$ case and consistent with the boundary conditions

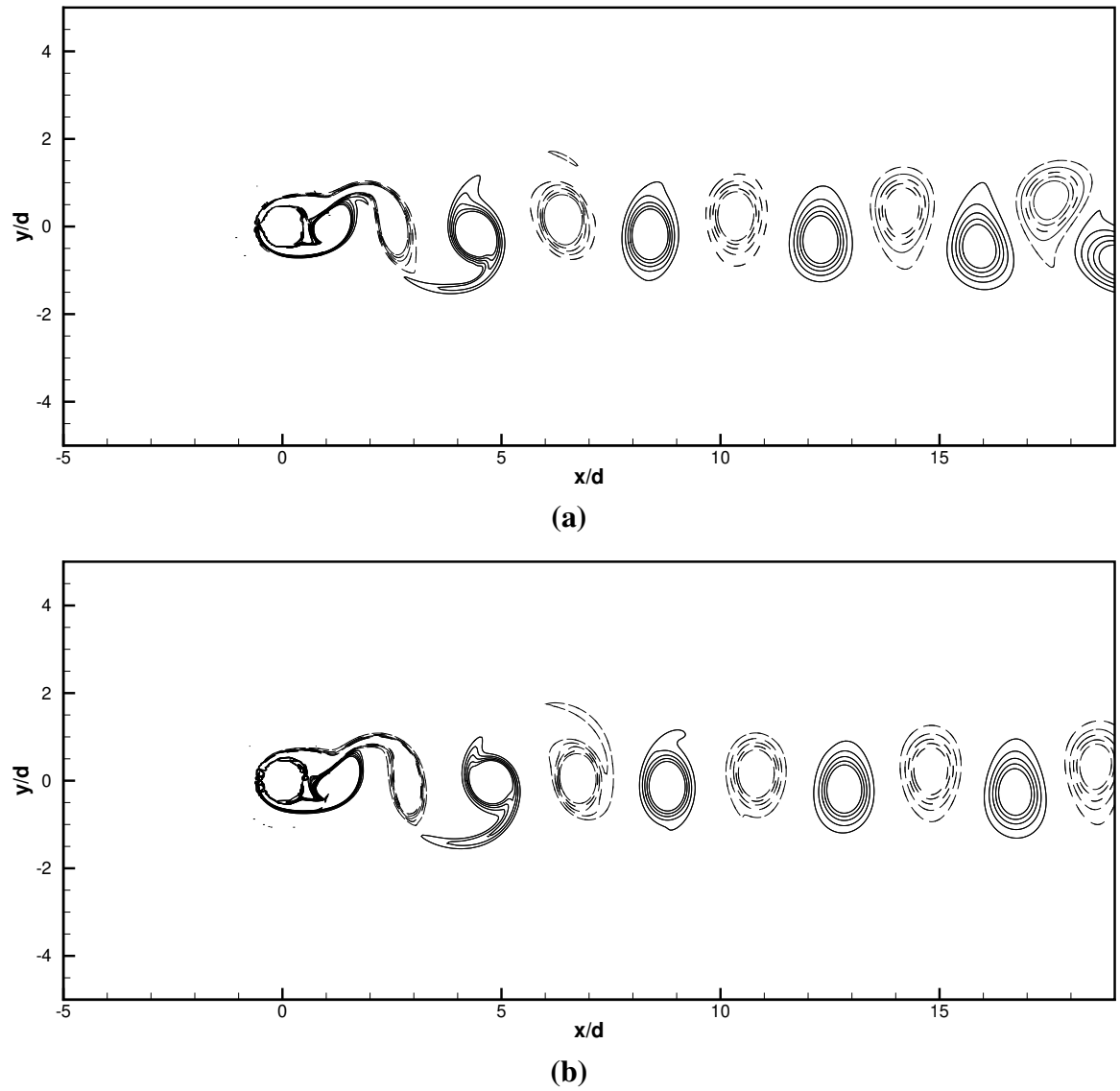

Figure 3.5: Comparison of vortex-shedding for $Re = 400$ between (a) freestream flow and (b) moving body at quasi-steady flow time $\tau = 96$.

enforced in the two cases. A clear difference in inlet pressure is observed between the two frames of reference for the $Re = 40$ cases shown in Figure 3.4(a). However, little difference in inlet pressure is present in the $Re = 400$ cases shown in Figure 3.7(a). In the wake, Figure 3.4(a) clearly shows that, for the case of steady flow, the pressure in the freestream flow case is higher than that of the moving flow case after $x/d \approx 10$ but, in the case of unsteady flow shown in Figure 3.7(a), the pressure fluctuates after $x/d \approx 5$. The same observation that the freestream flow case calculates a higher pressure is visible after $x/d \approx 10$.

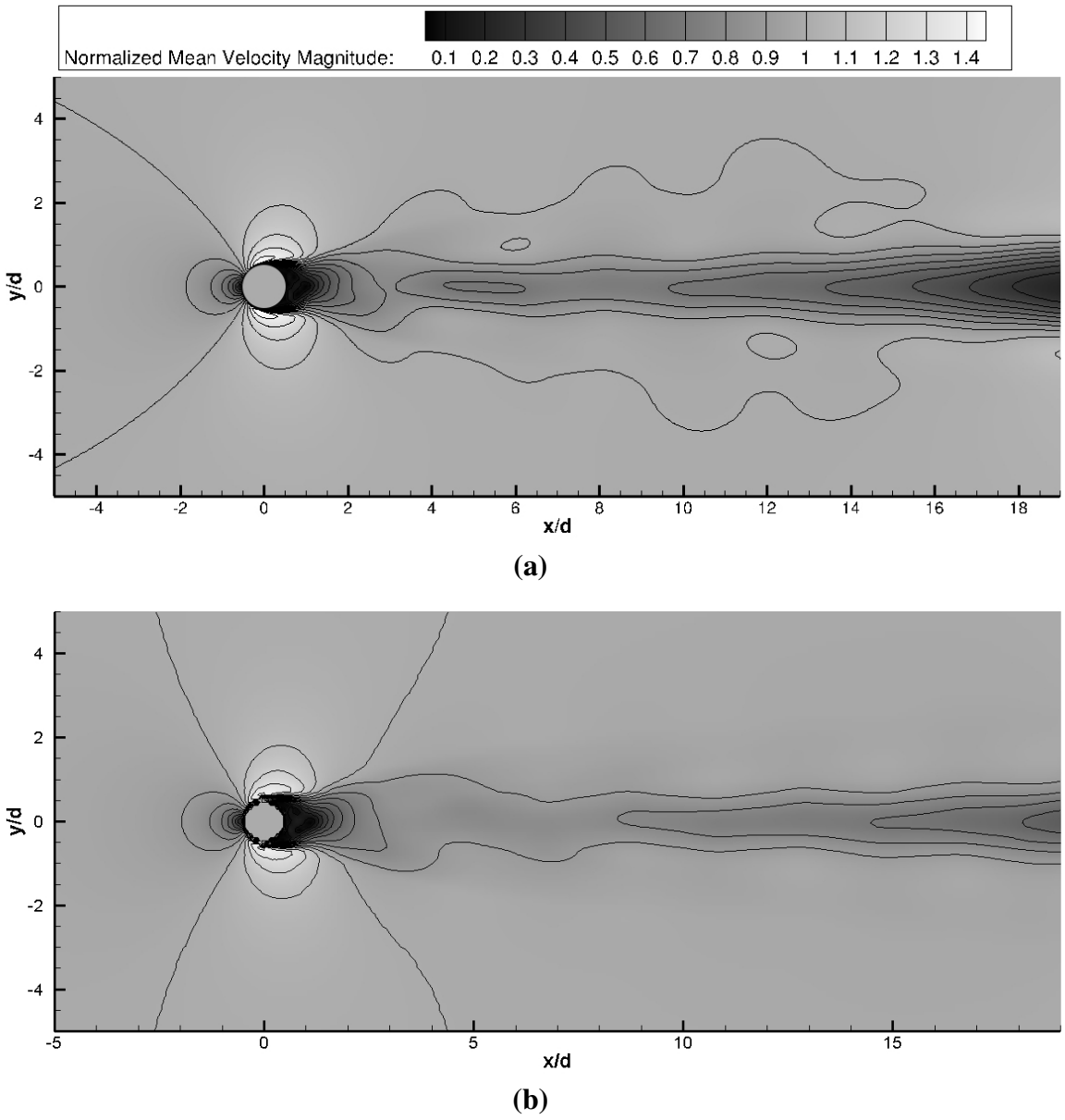

Figure 3.6: Comparison of time-averaged velocity for $Re = 400$ between (a) freestream flow and (b) moving body at quasi-steady flow time $\tau = 96$.

Meanwhile, Figure 3.7(b) illustrates the time-averaged centerline velocity for the body-fixed window. The dip in velocity magnitude occurs further downstream for the moving body, indicating that the vortex dipole pair (and secondary vortex street) forms and trails the cylinder at a further distance downstream compared to the simulation of the freestream flow. The trough in centerline velocity appearing at $x/d \sim 20 - 30$ compare well with the results of Jiang and

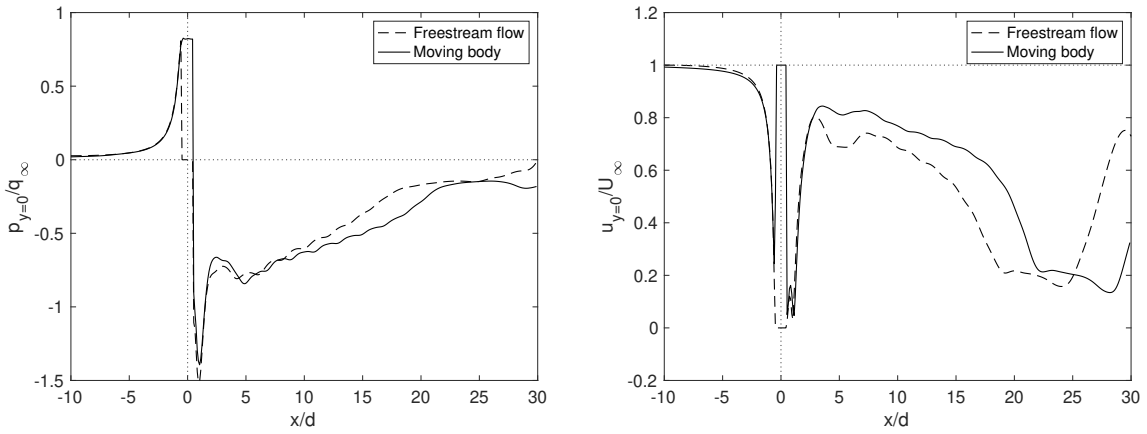

(a) **(b)**

Figure 3.7: Comparison of (a) centerline pressure and (b) centerline velocity across domain length for $Re = 400$.

Cheng [45] who noted that the transition to the secondary vortex street occurs within the region of $x/d \sim 20-30$ for $150 < Re < 1000$. Kumar and Mittal [29] and Jiang [30] suggested that this centerline velocity trough and the formation of the secondary vortex region is due to a convective instability of shear layers that causes an amplification of the perturbation energy in the region. Correspondingly, the moving body simulation should produce the trough at a distance further downstream than the freestream flow simulation, since the convective freestream velocity term is absent in the former. Additionally, the secondary vortex street is formed as the primary vortex street destabilizes and forms shear layers that roll up into packets of vorticity, which then convect downstream [46]. These vorticity clusters will merge with shear layers forming on the cylinder and result in a 2D turbulent flow in the region of the secondary vortex street [46].

In addition to Figure 3.7(b), velocity profiles comparing the wake of the stationary and moving body probed at $2d$, $7d$, and $17d$ downstream of the cylinder and at the end of the averaging time period are presented in Figure 3.8. The velocity profile for the stationary cylinder's wake indicates that the wake is widening downstream, as the peak at $17d$ is wider than the earlier peaks at $2d$ and $7d$. At $17d$, the wake velocity at $y \approx \pm 2$ increases slightly for the case of the freestream flow, indicating that the fluid in that region is accelerating. This acceleration corresponds to the start of the centerline velocity trough seen in Figure 3.7(b), which marks the

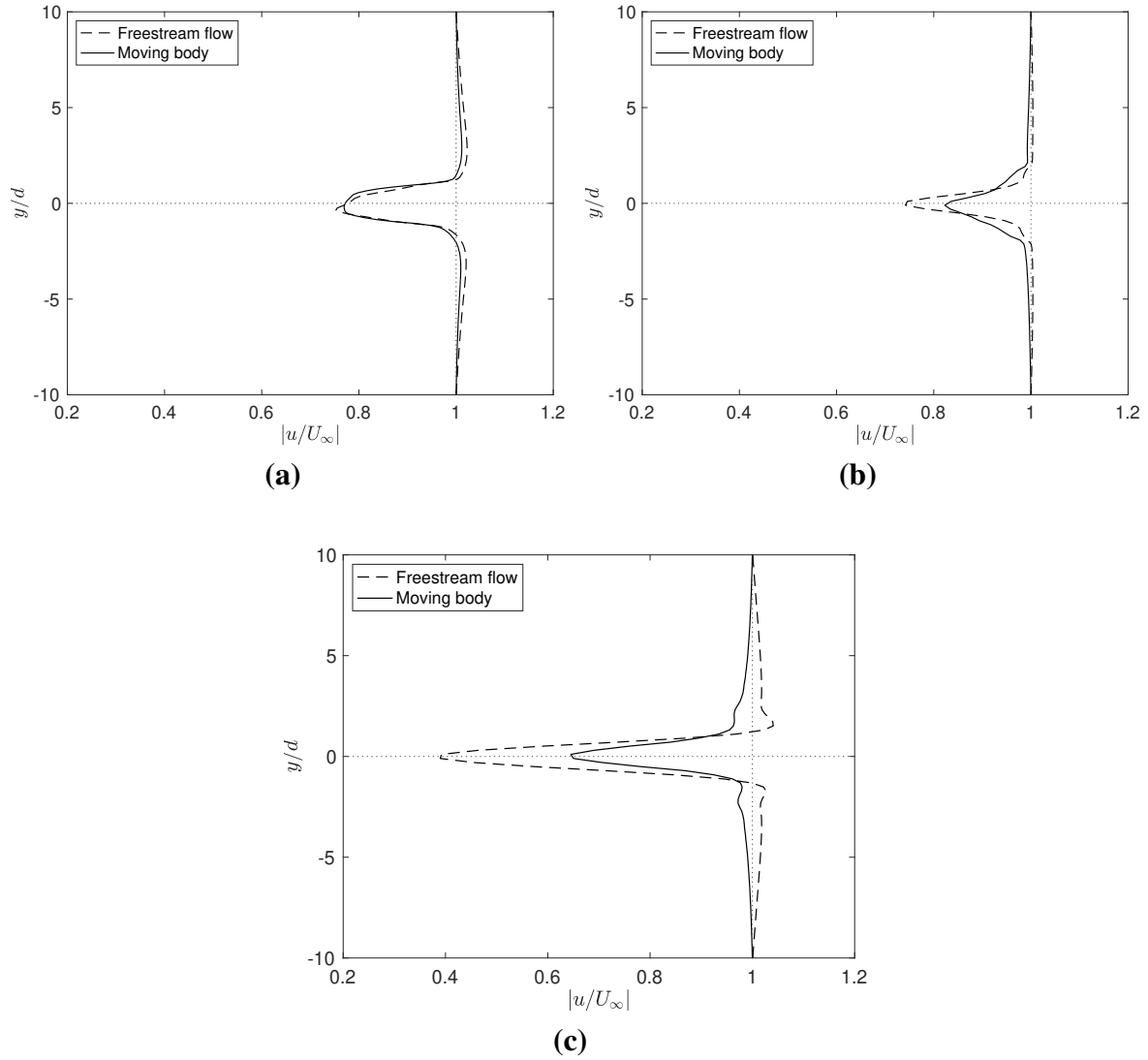

Figure 3.8: Velocity profiles at distances (a) $2d$, (b) $7d$ and (c) $17d$ downstream relative to cylinder at $Re = 400$.

start of transition to the secondary vortex street. In contrast, for the moving cylinder's wake, not only is the wake deficit smaller, the fluid also does not accelerate.

As explained by Dynnikova et al. [28], the region of high velocity seen for the freestream flow simulation in Figure 3.8(c) is due to the high dipole moment density in the secondary vortex street transition region, which has appeared at this downstream distance, $x/d \approx 17$ for the freestream flow, but not for the moving body. As the primary vortex street in the freestream flow case begins to break down, the separation between vortices decreases, as was shown in

Figure 3.5(a), causing the fluid in that region to be more influenced by multiple dipole moment clusters of vortices.

3.5 Entrainment

Fluid is entrained into the cylinder wake as it flows over the cylinder in the freestream flow case, or as the cylinder propagates in the moving body case. However, as shown in Figure 3.9(a), it is suspected that the stationary cylinder has a higher momentum flow imparted by the freestream velocity that is entrained by the von Kármán vortex street into the wake, which in turn convects the street downstream. Meanwhile, for the moving body, the surrounding fluid is stationary and has a lower momentum when entrained by the vortex street. In contrast to the convection of vortices downstream in the freestream flow, the cylinder moving in the quiescent ambiend fluid instead entrains some of the surrounding fluid into the wake to fill the void left by the cylinder, as illustrated in Figure 3.9(b).

This behavior will be further examined through calculation of mass and momentum fluxes

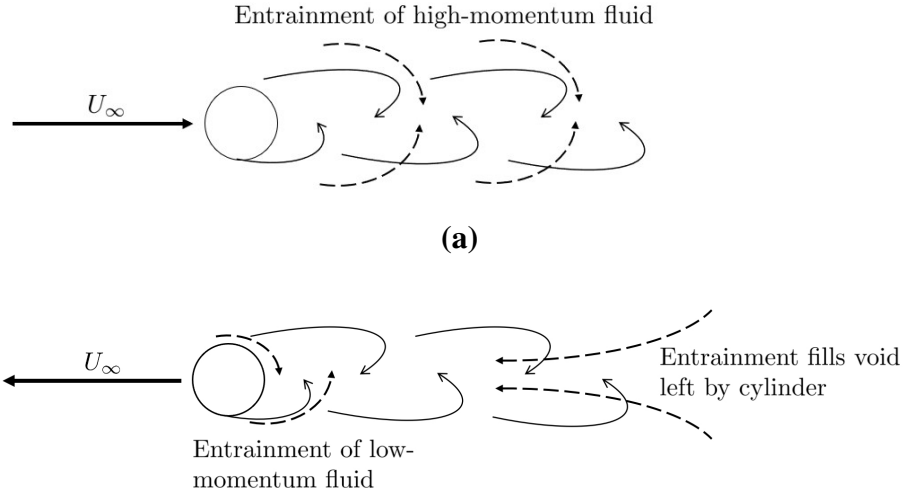

Figure 3.9: Entrainment of fluid in cylinder wake for (a) freestream flow over stationary cylinder and (b) cylinder moving in quiescent flow.

in both the body-fixed time-averaging and background-fixed time-averaging windows, as described in Section 2.7.3.

3.5.1 Body-Fixed Time-Averaging

The body-fixed window is shown in Figure 3.10. Mass and momentum fluxes across the top and bottom surfaces of the averaging window (stations (A) and (B), respectively,) as well as at four probe lines (stations (1)-(4)) are calculated across two periods of vortex-shedding, as described in Equation 2.14.

For an incompressible flow, the conservation of mass in differential form is $\nabla \cdot \mathbf{u} = 0$. Integrating over the entire volume and applying the Gauss Divergence theorem,

$$\int_V (\nabla \cdot \mathbf{u}) dV = 0 \Longrightarrow \int_S \mathbf{u} \cdot d\mathbf{S} = 0$$

This means that, over a rectangular control volume, the mass flux horizontally across control surfaces can be represented by $\int u dy$ and the mass flux vertically across horizontal control surfaces by $\int v dx$. Hence, the velocity component u is plotted at stations (1)-(4) while the velocity component v is plotted for horizontal lines at stations (A) and (B).

Assuming that body forces (e.g., gravity) are negligible, the integral form of the Navier-Stokes

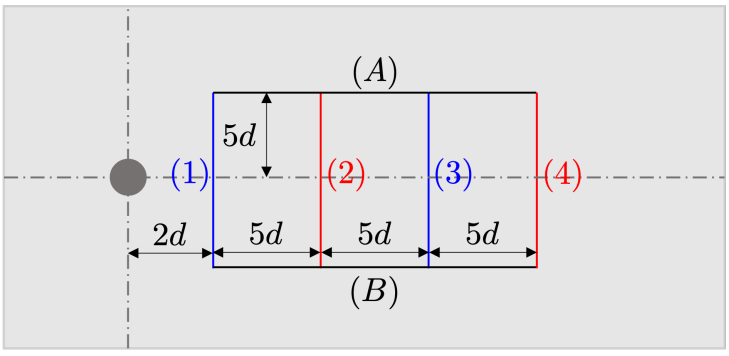

Figure 3.10: Probe lines for body-fixed time-averaging. The window is fixed relative to the cylinder at the indicated distance and translates together with the cylinder in the moving case.

equations describing momentum conservation for the same incompressible flow is

$$\int_V \frac{\partial(\rho u_i)}{\partial t} dV + \int_A (\rho u_i \mathbf{u} - \mu \nabla u_i) \cdot d\mathbf{S} = -\int_V \nabla_i p dV \tag{3.1}$$

Expanding Equation 3.1 results in Equation 3.2 for the $x-$component of the momentum.

$$\int_V \frac{\partial(\rho u)}{\partial t} dV + \int_S (\rho u \mathbf{u} - \mu \nabla u) \cdot d\mathbf{S} = -\int_V \frac{\partial p}{\partial x} dV \tag{3.2}$$

From the second term $\int \rho u \mathbf{u} \cdot d\mathbf{S}$, $\int u^2 dy$ measures the $x-$momentum fluxes across vertical control surface, while $\int uv dx$ measures the $x-$momentum fluxes across horizontal control surface. Likewise, the $y-$momentum can be expanded from Equation 3.1 to give Equation 3.3, where the $y-$momentum fluxes across vertical control surface is given by $\int uv dy$ and across horizontal control surface by $\int v^2 dx$.

$$\int_V \frac{\partial(\rho v)}{\partial t} dV + \int_S (\rho v \mathbf{u} - \mu \nabla v) \cdot d\mathbf{S} = -\int_V \frac{\partial p}{\partial y} dV \tag{3.3}$$

Therefore, the components u^2 and uv are plotted across stations (1)-(4) while the components uv and v^2 are plotted at stations (A) and (B) to further examine the entrainment and mixing behaviors of the vortex street. If Galilean invariance between the stationary and moving frames of reference is satisfied, then Equations 3.2 and 3.3 should produce similar results across both reference frames. If large differences are present in the momentum terms, it suggests that the two reference frames are not invariant because the governing equations are [47].

After subtracting the freestream velocity, the u, uv, and u^2 terms should produce the same result, since the removal of freestream velocity is assumed to account for the difference in boundary conditions for the $x-$axis. As the same boundary conditions are prescribed to both freestream flow and moving cylinder simulations in the $y-$axis the vertical velocity components v and v^2 are also expected to be similar. However, in the stationary cylinder case, the term $\partial p/\partial x$ is non-zero due to pressure gradient applied from the inlet to the outlet to drive the freestream flow. The pressure gradient is equal to zero for the moving cylinder case as the background flow is quiescent. With the window chosen in Figure 3.10, any differences in the mass and momentum fluxes will hence likely be due to a difference in entrainment behavior of the

wake. Additionally, in the case of the *uv* term, using the freestream flow scenario (body-fixed reference frame) possibly results in an overprediction of mixing.

3.5.2 Mass Entrainment

Figure 3.11 illustrates the time-averged velocity component v in the body-fixed window for stations (A) and (B). Figures 3.11(a) and 3.11(b) are symmetrical about the $x-$axis and demonstrate mass flux out of the control volume (bounded by stations (A) and (B), as well as stations (1) and (4) in Figure 3.10) for both the top and bottom surfaces. This indicates that the wake is expanding, which is in agreement with Figure 3.6. Trapezoidal integration of Figure 3.11 over both stations (A) and (B) shows that the value of $\int v dx$ differs across the reference frames by 6.25% with the moving body simulation calculating a higher value of mass flux out. This can also be deduced from a visual inspection of Figures 3.11(a) and 3.11(b), which appear vastly different. Specifically, the case of moving body has a higher and sharper peak further downstream compared to the case of the freestream flow.

Turning now to the horizontal component of mass flux, Figure 3.12 illustrates the time-averaged x-component of velocity, u, at stations (1)-(4) downstream of the cylinder. The negative values

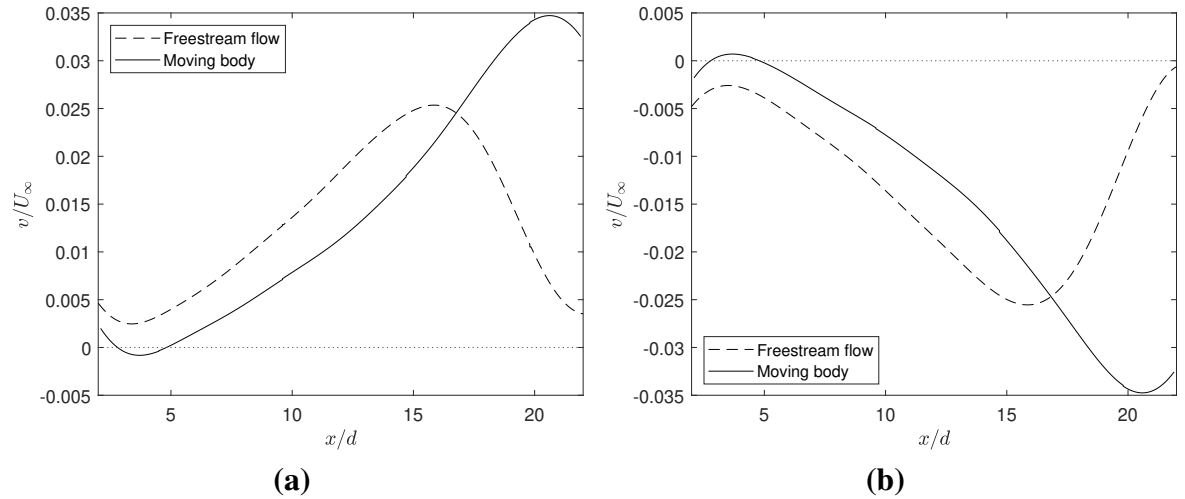

Figure 3.11: Velocity component v time-averaged in body-fixed window for probe lines (a) $7d$ above the cylinder and (b) $7d$ below the cylinder.

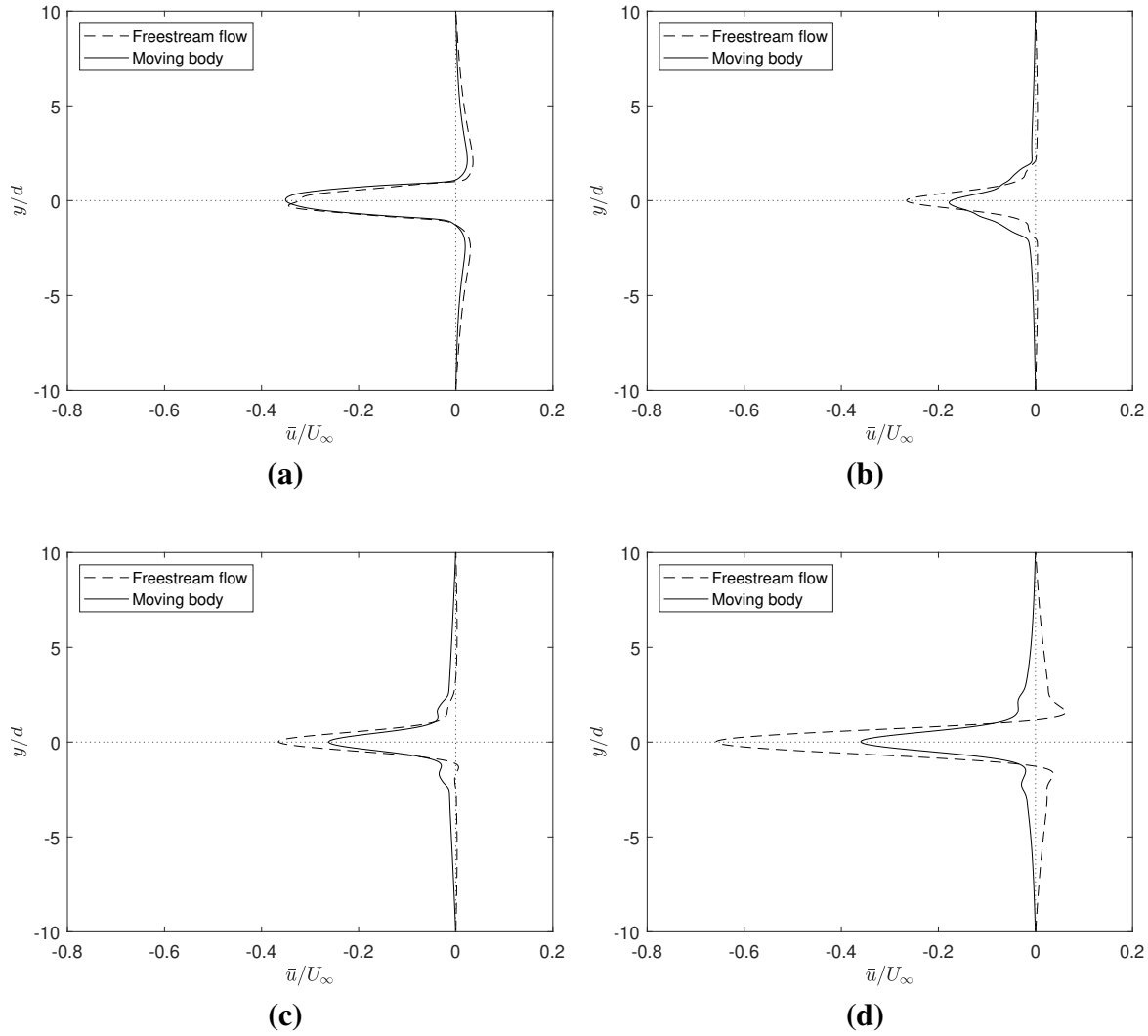

Figure 3.12: x-component of velocity, u, at distances (a) $2d$, (b) $7d$, (c) $12d$ and (d) $17d$ downstream relative to cylinder at $Re = 400$.

of velocity indicate that fluid is being entrained by the cylinder translating in the $-x$ direction. From Figure 3.12, the mass flow first decreases at stations (1) and (2) before an increase in the velocity presents at stations (3 and (4), which is a similar result seen in Figure 3.7(b) for velocity magnitude. It should be noted that, in contrast to the vertical mass flux, the peak deficit of the wake is higher in the freestream flow case for all stations (2)-(4) except station (1), where both reference frames show similar velocity, u.

Calculating the value of $\int u dy$ using trapezoidal integration of the plots in Figure 3.12 yield

Table 3.5: Mass flux $\int udy$ across vertical control surfaces for $Re = 400$

Control surface	Freestream flow	Moving body
1	-0.0012	-0.0021
2	-0.0017	-0.0024
3	-0.0025	-0.0030
4	-0.0036	-0.0040

the mass flux across the four control surfaces, which is summarized in Table 3.5. The negative values indicate that fluid is going opposite to the direction of freestream flow. Evidently, the magnitude of mass flux increases downstream of the cylinder, indicating that entrainment increases with distance from the cylinder. Additionally, the magnitude of mass flux for the moving body is significantly higher than for the freestream flow (10-75% difference). This supports the theory put forward in Figure 3.9 where the moving cylinder is entraining fluid into its wake to fill the void it leaves, which does not happen for the case of freestream flow. In the far wake, the difference between frames shrinks as the cylinder's effect is less prominent.

3.5.3 Axial momentum Entrainment

Figure 3.13(a) presents the time-averaged uv term corresponding to the axial component of momentum for the body-fixed window for the probe line at station (A) while Figure 3.13(b) presents the same term for the probe line at station (B). Note that the momentum fluxes for the two reference frames are in opposite directions from each other and the magnitude of the momentum flux in the freestream flow simulation is approximately twice that of the moving body simulation. The value of $\overline{uv}$ across control surface (A) for the freestream flow simulation has a lower peak magnitude that appears further upstream compared to the moving cylinder simulation, which instead shows a dip before increasing further downstream, as shown in Figure 3.13(a). Across control surface (B) this observation is likewise repeated as shown in Figure 3.13(b).

Meanwhile, Figure 3.14 illustrates the time-averaged axial component of momentum, represented by u^2, at stations (1)-(4) downstream of the cylinder. Both freestream flow and

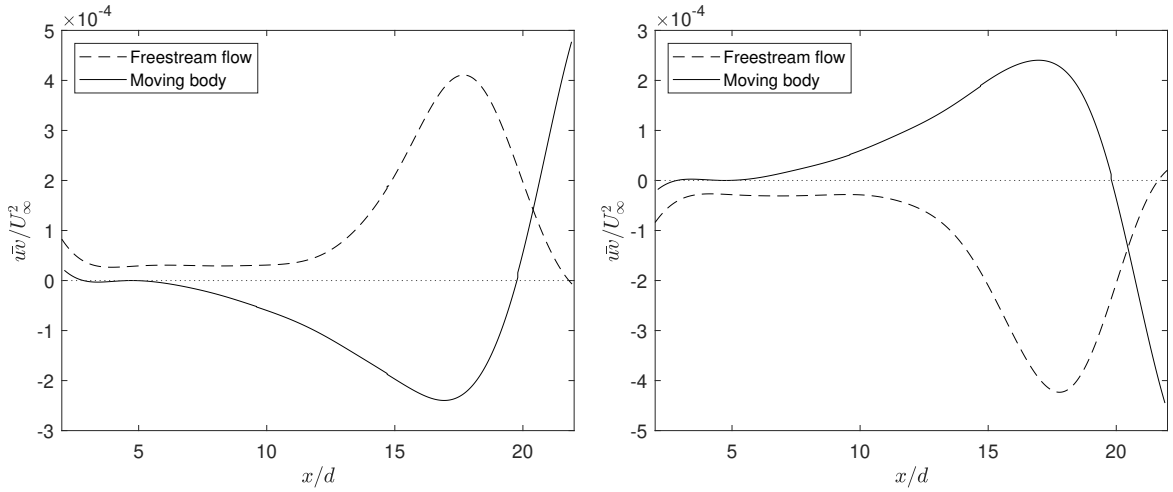

Figure 3.13: $x-$momentum term uv time-averaged on a probe line (a) $5d$ above and (b) $5d$ below the cylinder.

moving cylinder simulations show two distinct peaks above and below the $y = 0$ line, which then diffuse and combine into a single peak. For stations (1) and (2), which correspond to $2d$ and $7d$ downstream of the cylinder, the two peaks are obvious and similar for both the freestream flow and the moving body. These peaks likely represent the vortices being shed from the cylinder. However, at station (3), $12d$ downstream from the cylinder, the peaks of the freestream flow have already merged together, whereas that of the moving cylinder simulation are still distinct. This possibly indicates that the momentum transfer to the surrounding fluid is quicker for the case of the freestream flow, even though the vortex strengths might look similar in Figure 3.5. Also, the fluid in the wake of the cylinder subject to freestream flow accelerates faster, as clearly seen from Figure 3.14(d).

Jiang and Cheng [45] previously noted the presence of two-layered "merged" vortices in the transition region, which is reflected by the appearance of a single sharper peak instead of two flatter peaks in the velocity magnitude. The coalescing of the two peaks from Figure 3.14(b) to 3.14(c) for the freestream flow and from Figure 3.14(c) to 3.14(d) for the moving cylinder, as well as the sharp increase in the u^2 term for the freestream flow in Figure 3.14(d) indicates that the location $x/d \approx 17$ falls within the transition region from primary to secondary street.

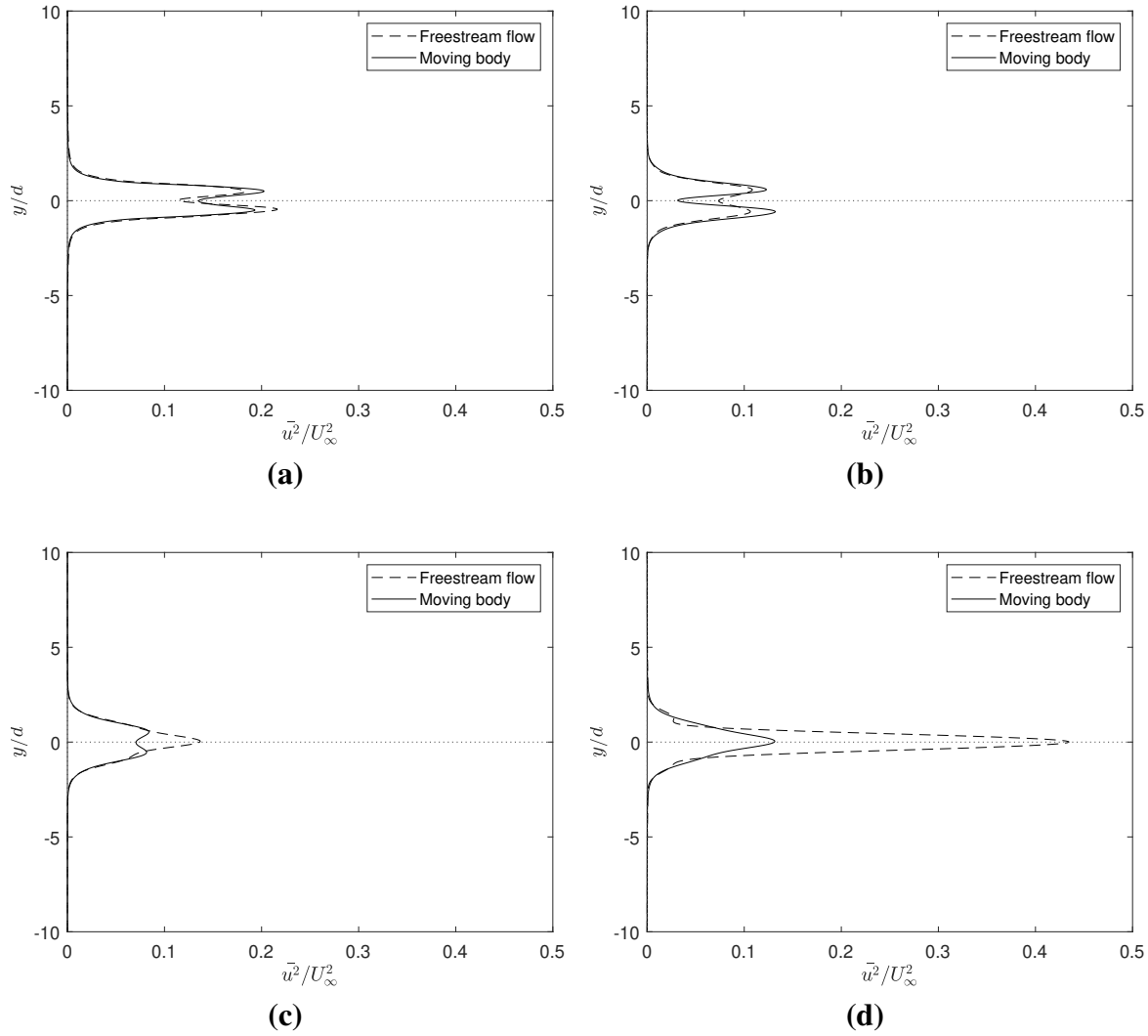

Figure 3.14: u^2 term at distances (a) $2d$, (b) $7d$, (c) $12d$ and (d) $17d$ downstream relative to cylinder at $Re = 400$.

3.5.4 Normal momentum Entrainment

Figure 3.15 displays the time-averaged normal component of momentum for the top and bottom stations (A) and (B) represented by the term v^2. As expected, since the wake is symmetrical, the momentum fluxes on top and bottom stations are effectively identical. It can be observed from Figure 3.15 that the moving body simulation has a much higher peak value that appears further downstream compared to the freestream flow simulation. Also, performing trapezoidal integration over the control surface, the moving body simulation not only has a

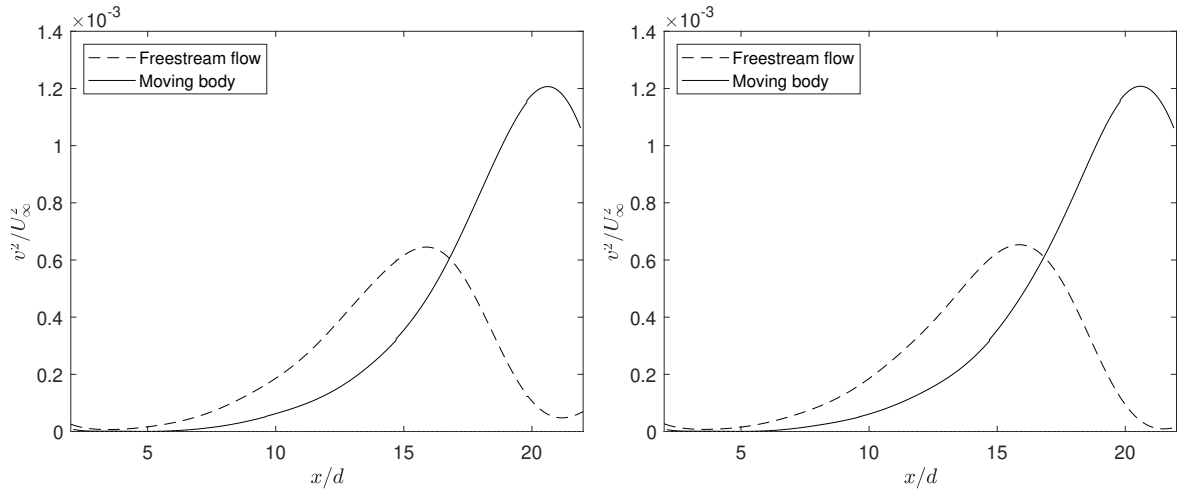

Figure 3.15: $y-$momentum term v^2 time-averaged on a probe line (a) $5d$ above and (b) $5d$ below the cylinder.

greater momentum flux after $x/d \approx 17$, but in total as well.

Figure 3.16 illustrates the time-averaged normal component of momentum represented by the term uv at stations (1)-(4) downstream of the cylinder. Common between the two cases are two peaks in opposite directions at station (1) $2d$ downstream of the cylinders, likely representing the opposite sign vortices being shed from the cylinder. For both peaks,the magnitude of uv is higher in the moving body case. As the flow progresses downstream to station (2) and then to station (3), the two peaks of momentum begin to flatten and turn into one dominant peak, for which the sign is opposite between the freestream flow and moving body, and one smaller peak. Like the u^2 term shown in Figure 3.12(b), the dominant peak is possibly indicative of the start of the transition region, where the vortices are merging into a single two-layer vortex [45]. Finally, at station (4), four distinct peaks appear in opposite directions for the freestream flow, suggesting that the secondary vortex street is formed around this area [45]. In contrast to the observation at station (1), the peaks in the freestream flow case of station (4) are sharper and higher than that of the moving cylinder.

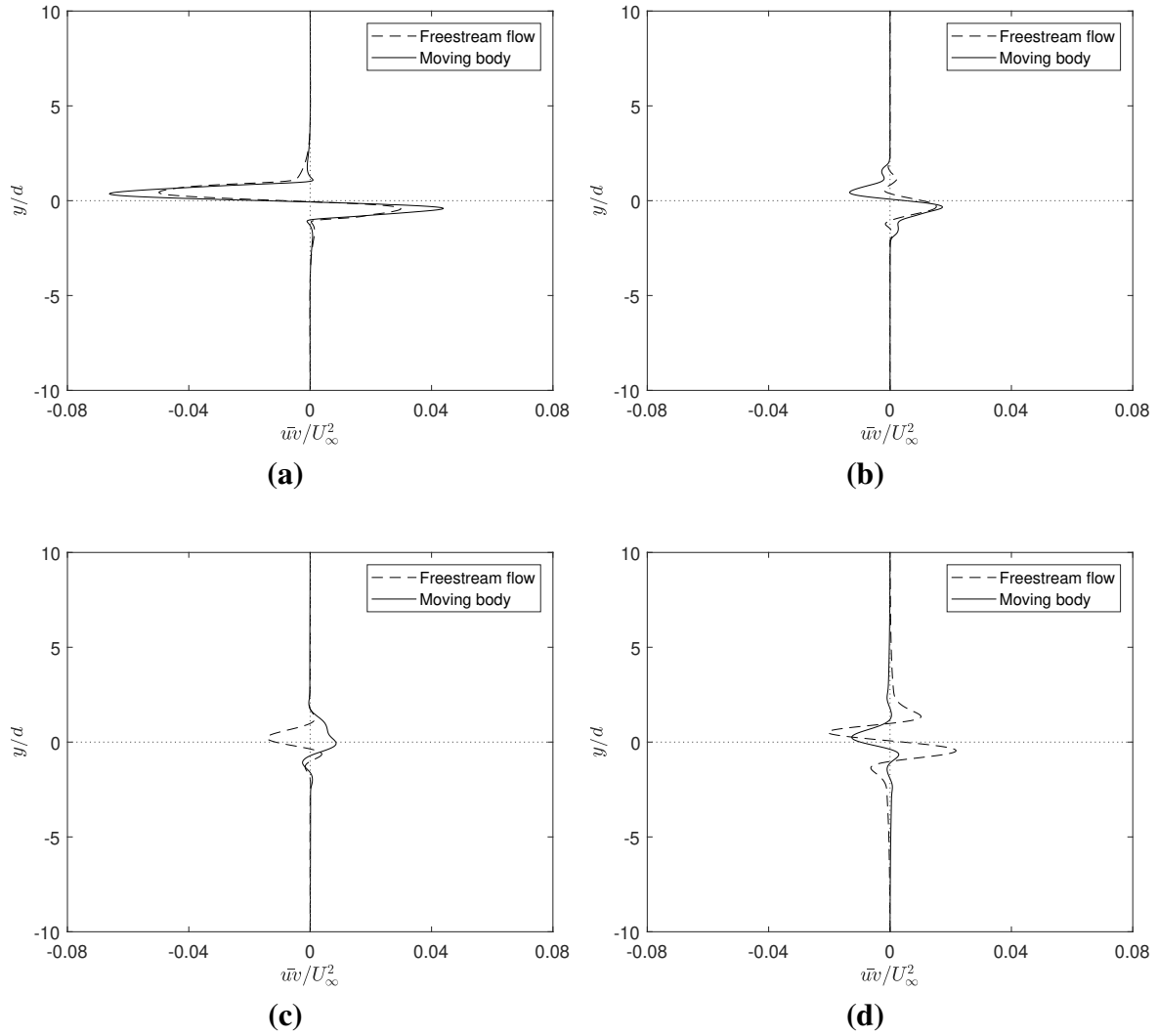

Figure 3.16: *uv* term at distances (a) $2d$, (b) $7d$, (c) $12d$ and (d) $17d$ downstream relative to cylinder at $Re = 400$.

3.5.5 Background-Fixed Averaging

A schematic of the background-fixed averaging is shown in Figure 3.17. As described in Section 2.7.3, the cylinder translates away from the probe volume and the fluid in the probe volume is observed over time. This background-fixed averaging procedure is similar to the particle-image velocimetry (PIV) experimental technique, which derives a velocity field from the movement of tracer particles within a window fixed to the background fluid [48]. The technique is often used to investigate vorticity and other vector properties of the fluid. By

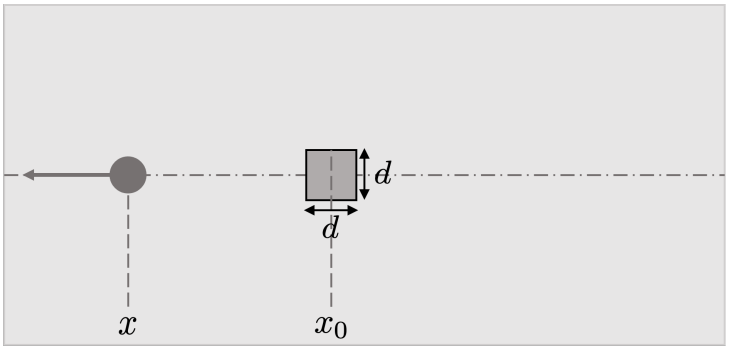

Figure 3.17: Schematic of background-fixed averaging. Quantities were averaged spatially over the dark grey square box of $1d \times 1d$ at every timestep. At $t = 0$, the cylinder is overlaid onto the box (i.e., $x - x_0 = 0$).

summing up the momentum terms over the probe volume, the total pressure, shear, and viscous force on the fluid can be derived.

Here, fluid velocity is spatially-averaged over a fixed volume of $1d$ on all four sides. The procedure in Equation 2.15 starts at the quasi-steady state when the cylinder is directly inlaid on the probe volume. As explained in the preceding section 3.5.1, the momentum fluxes characterized by u^2, uv, and v^2 are of interest here as they represent entrainment and mixing for the fluid. In the freestream flow case, the freestream velocity is removed from the plot by means of plotting $u_a = u - U_\infty$. Additionally, two more quantities, namely the vorticity, $\omega = \nabla \times \mathbf{u}$, and the wake momentum deficit, $u(U_\infty - u)$, are investigated as their time-histories characterize the decay of the wake. In the case of the freestream flow, the wake momentum deficit is directly given by $u(U_\infty - u)$, whereas, in the moving cylinder case, the wake momentum deficit is $-u^2$, since $U_\infty = 0$. The results for the freestream flow case here were extracted from an extended domain downstream of the cylinder in order to match the averaging for the moving cylinder case.

The u^2-component of velocity in Figure 3.18(a) shows a large increase around $(x - x_0)/d \approx 15$ and 20 for the freestream flow and moving body cases, respectively. This indicates that the fluid is accelerating around this region before slowing down again at around $(x - x_0)/d \approx 20$ and 30 for the freestream flow and moving body cases, respectively. Observing the contours of u from Dynnikova et al. [28] and Jiang and Cheng [45], this behavior is indicative of the transition region where the large vortex dipole cluster is forming and inducing the secondary vortex street.

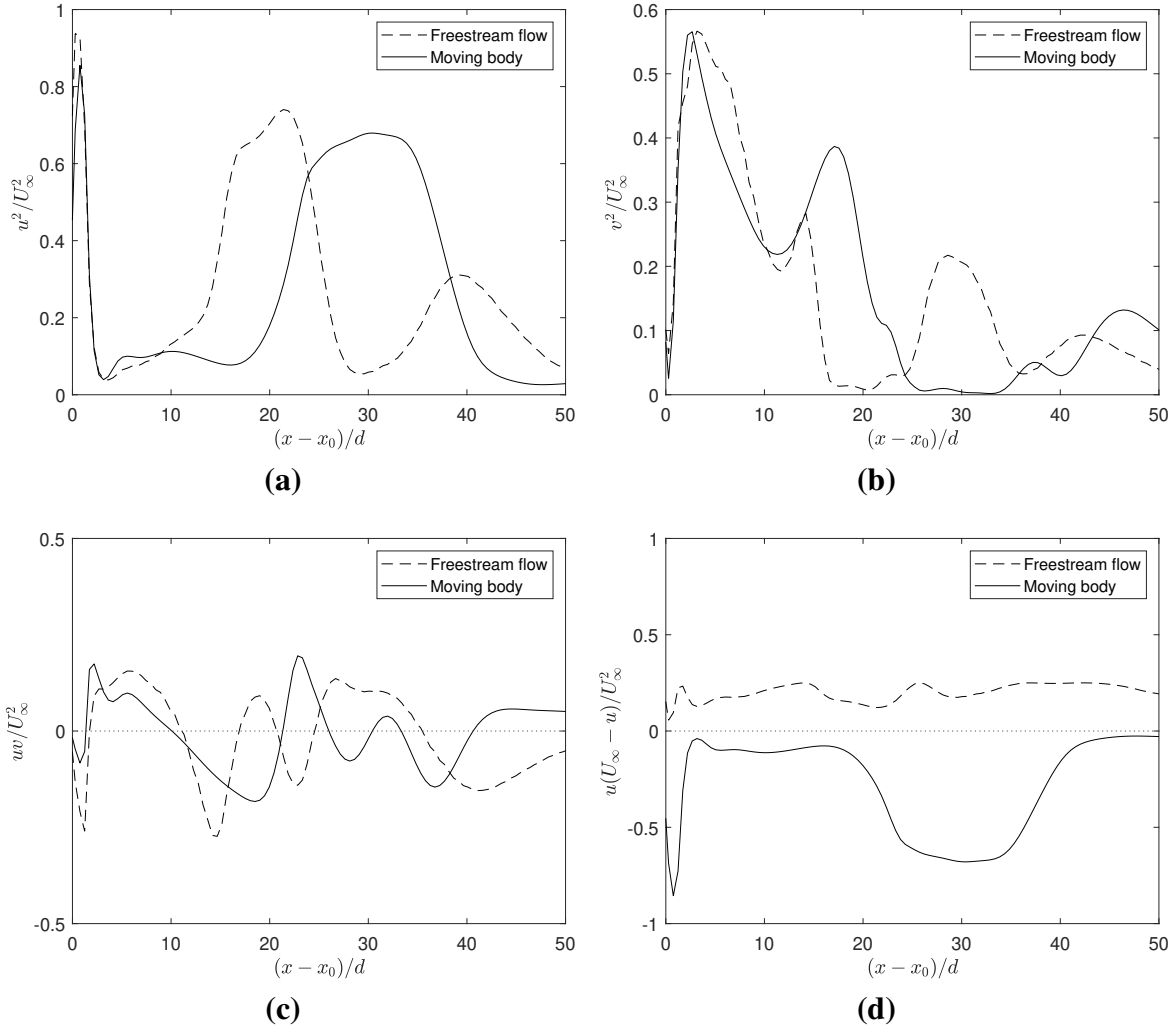

Figure 3.18: Spatially-averaged quantities (a) u^2, (b) v^2, (c) uv, and (d) $u(U_\infty - u)$ in background-fixed window over time.

From its location of the acceleration region, the moving body wake breaks down into secondary vortices at a later distance than the freestream flow. The second peak at $(x-x_0)/d \approx 40$ for the freestream flow may be due to additional momentum entrained by the secondary vortex street, but further work out of the current scope is needed to confirm this.

In Figure 3.18(a), the peak at $(x-x_0)/d \approx 20$ and 30 is followed by a trough at $(x-x_0)/d \approx 30$ and 50 for the freestream flow and moving body cases, respectively. On the plot of v^2 in Figure 3.18(b), the troughs corresponds to peaks at the same locations. This possibly suggests that, at these locations, the vertical momentum component is greater than the horizontal, a behavior

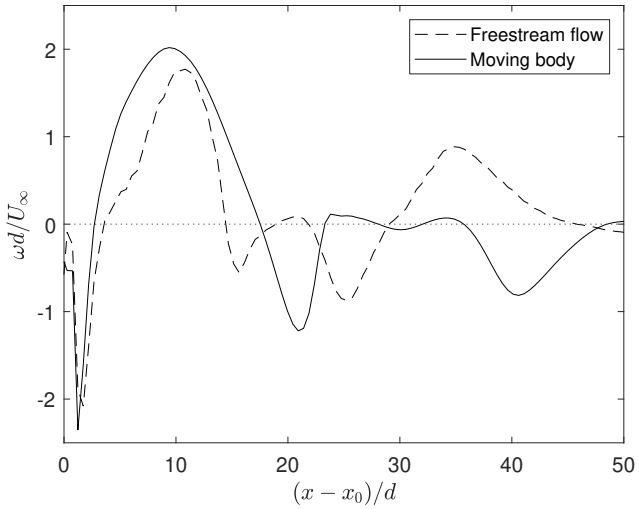

Figure 3.19: Spatially-averaged vorticity in background-fixed window over time.

that is also observed in the near-wake of the cylinder where the primary vortex street is formed.

Examining the v^2 plot, the vertical component of velocity shows a decaying oscillatory pattern that is consistent with vortex-shedding, before a sharp dip at $(x-x_0)/d \approx 20$ and 30 for the freestream flow and moving cylinder cases, respectively. Consistent with observations in the body-fixed averaging study, the moving body's wake takes longer to produce the secondary vortex street compared to the freestream flow case.

Regarding the decay behavior of the wake, Figure 3.18(c) shows that the wake decays quicker in the moving body case than the freestream flow case as the graph approaches zero faster for the former. This observation is corroborated by the vorticity plot in Figure 3.19, which shows the moving body vorticity approaching zero more quickly and having a faster decay of the oscillation.

Figure 3.18(d) shows a much larger $x-$momentum deficit for the moving body simulation compared to the freestream flow simulation, along with a sharp dip between $20 < (x-x_0)/d < 30$ that is not observed for the freestream flow. Also, the momentum deficit term of the moving cylinder eventually disappears far downstream at $(x-x_0)/d \approx 50$, while the freestream flow momentum deficit term does not return to zero.

As described in Sections 3.3-3.4, zero pressure boundary conditions were enforced at the left and right boundaries of the moving domain. Meanwhile, for the freestream flow, the upstream velocity is fixed, so a pressure gradient will form from the inlet to the outlet to drive the flow. For momentum to be conserved over the entire domain in the manner described by Equation 3.2, the introduction of a pressure gradient will likely result in changes in the other terms, such as the convective fluxes. This possibly accounts for the different fluid properties shown in Figures 3.11-3.19 compared to the moving body simulation.

3.6 Discussion

As the Navier-Stokes equations are Galilean-invariant [6, 47], fluid motion, which is governed by those equations, should likewise also be Galilean-invariant. However, the results presented in this thesis do not support that conclusion. Hence, several explanations are proposed to address the discrepancy in the unsteady vortex-shedding behavior and forces between the stationary and the moving frames of reference for the cylinder.

3.6.1 Effect of 3D

Williamson [17] observed that the 3D coefficients of lift and drag are significantly lower than that of 2D cases at Reynolds numbers above $Re \approx 300$, as the wake will become 3D due to bifurcations caused by wake velocity fluctuations [49]. The 3D behavior of the wake causes changes in the pressure distribution over the cylinder, thus affecting the aerodynamic forces

Table 3.6: Values of mean c_d and St calculated in 3D at $Re = 400$

	2D	3D	% difference
Freestream $\overline{c_d}$	1.4196	1.3970	1.6178
Freestream St	0.2167	0.2083	4.0326
Moving body $\overline{c_d}$	1.1768	1.1716	0.4438
Moving body St	0.2007	0.2082	-3.6023

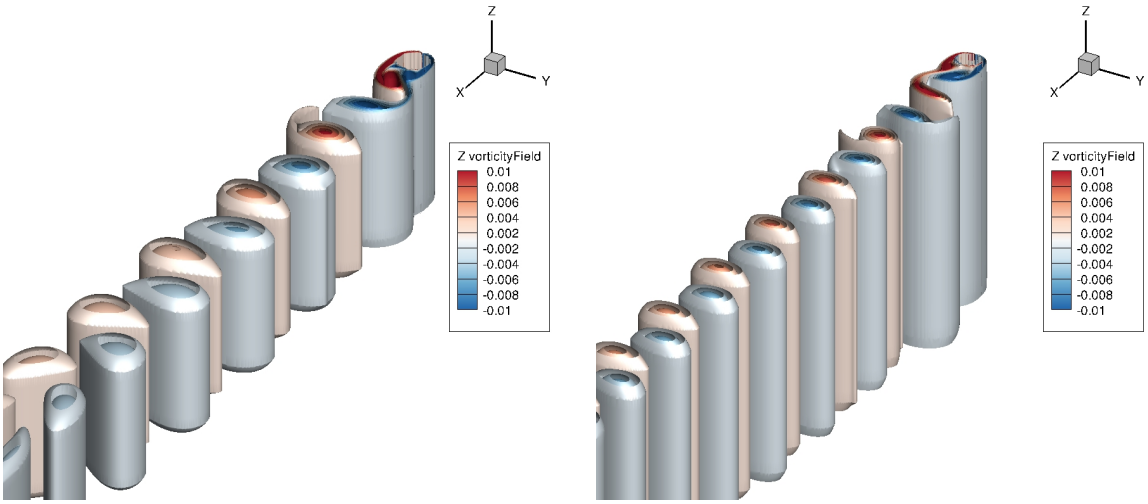

(a) **(b)**

Figure 3.20: Isosurfaces of vorticity calculated in 3D simulation for (a) freestream flow and (b) moving body.

over the cylinder [1]. Hence, additional simulations were run in 3D to investigate whether 3D effects were significant at $Re = 400$ to account for the differences.

Table 3.6 summarizes the drag coefficient and Strouhal number calculated from 2D and 3D simulations. Note that the 3D results in Table 3.6 were obtained using a CFL number of 0.6, for which the upwind scheme is more accurate (see Section 2.5), to keep the computational cost tractable. The same were applied on the 2D cases for consistency, so the values for 2D here are different from the values presented in the preceding sections even though the rest of the case setup is identical to those described in Chapter 2. Periodic boundary conditions in the $z-$axis were used for the 3D simulation with 21 layers of uniform-thickness cells for a total thickness of $0.6d$.

From Table 3.6, the 3D effects were negligible with less than 2% and 4% differences for the drag coefficient and Strouhal number, respectively. However, the values still compare well with experimental and previous computational data given in Table 3.4. Furthermore, from Figure 3.20, the vortex street that forms downstream of both cylinders is laminar and free of 3D and end effects. Hence, the 3D effects can justifiably be neglected in the 2D simulations.

3.6.2 Effect of Added Mass

The effect of added mass has been suggested in Refs. [11, 12], as it accounts for the acceleration of flow and is usually taken into consideration for accelerating bodies. Hence, an additional simulation was performed using the properties of water at $Re = 400$ to determine if any significant added mass effect is present in the moving body simulation compared to the stationary body simulation. As the density of water is much higher than the density of air, any added mass effects will be amplified at the same Reynolds number. To reduce computational cost, the upwind scheme with CFL number 0.6 was used for both air and water simulations.

The drag coefficient and Strouhal number obtained from the simulations in water and air are summarized in Table 3.7, which show differences between 1-3%. Since the differences are negligible, the added mass effect in simulation can be neglected.

Table 3.7: Values of $\overline{c_d}$ and St calculated using air and water at $Re = 400$

	Air	Water	% difference
Freestream $\overline{c_d}$	1.4154	1.3962	1.3565
Freestream St	0.2153	0.2164	-0.5109
Moving body $\overline{c_d}$	1.2884	1.2500	2.9804
Moving body St	0.2058	0.1998	2.9155

3.6.3 Effect of Compressibility

The effect of using a compressible solver rather than the incompressible solver was investigated to evaluate the pressure waves that form upstream due to the translating cylinder. This could have resulted in the compressibility being significant, which an incompressible solver cannot capture. Due to high computational costs and potential instability associated with the central scheme in the compressible solver, upwind scheme with CFL number 0.6 was used for both incompressible and compressible cases. However, Table 3.8 illustrates that the compressibility effect is insignificant with differences of 3% or less between the drag coefficient and Strouhal number of the two solvers.

Table 3.8: Values of c_d and St calculated with compressible solver at $Re = 400$

	Incompressible	Compressible	% difference
Freestream c_d	1.4154	1.4077	0.55
Freestream St	0.2153	0.2082	3.41
Moving body c_d	1.2884	1.2467	3.35
Moving body St	0.2058	0.2041	0.83

3.6.4 Effect of Timestep Size

In Section 3.1, grid independence was investigated by holding CFL constant and refining the grid, which required timestep to also be refined together. Another factor that could possibly affect the result is the CFL number, which can be seen from comparing the results in Sections 3.6.1-3.6.3 to the results presented at the start of this chapter. This is because, in the case of the moving cylinder, the overset interface is moving along the background mesh. Therefore, if the CFL number is too small, there could be no changes perceived by the background mesh if the overset patch does not move a sufficient distance every timestep, as illustrated in Figure 3.21.

Consider a non-dimensional rate, Ω, at which information is passed along the overset interface, where

$$\Omega = U_\infty \Delta t / \Delta x_i$$

Δx_i is the cell spacing at the overset interface as shown in Figure 3.21. Since

$$\text{CFL} = U_\infty \Delta t / \Delta x$$

Ω can be rewritten as

$$\Omega = \text{CFL} \cdot \left(\frac{\Delta x}{\Delta x_i} \right)$$

Take for example $\Delta x / \Delta x_i \approx 5/3$, for CFL = 0.06, $\Omega \approx 0.1$, while for CFL = 0.6, $\Omega \approx 1$. For the higher CFL = 0.6, the overset cell that has information passed to the background mesh changes every timestep. In contrast, for the lower CFL = 0.06, the cell that passes information from the overset to the background mesh only changes every 10 timesteps. This possibly indicates that the background mesh is not updating quickly enough if the CFL number is too small.

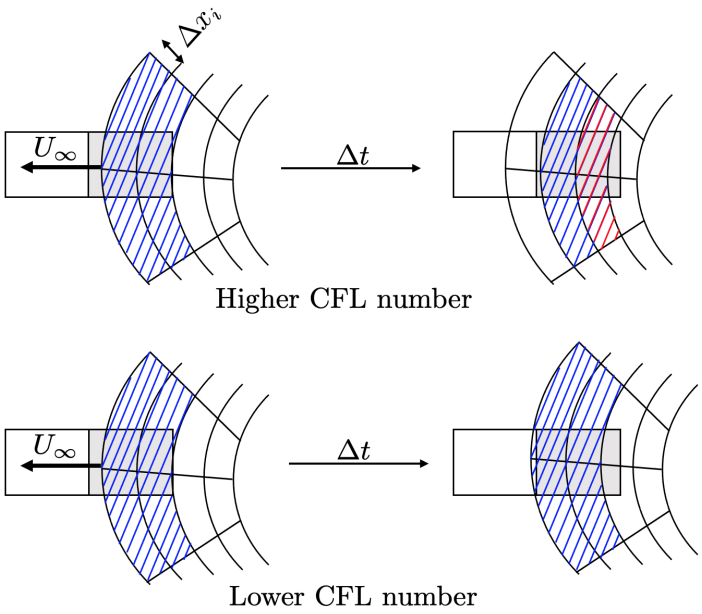

Figure 3.21: Schematic of overset interpolation for different CFL number. For higher CFL numbers, new data (shaded in red) is interpolated to the background mesh cell (shaded in grey) at every timestep. For lower CFL numbers, it takes several timesteps before data from new overset cells is transferred to the background mesh cell.

Hence, a set of simulations was also carried out using the central scheme with a higher CFL = 0.6 to demonstrate the effect of the timestep size choice on the forces and the wake of the cylinder in both reference frames.

Figure 3.22 presents the von Kármán vortex street for the freestream flow and moving cylinder calculated using the higher CFL number of CFL = 0.6. This can be contrasted with Figure 3.5, which illustrates the same calculation using a lower CFL number of CFL = 0.06. While there is no noticeable difference in the pattern for the moving cylinder, the vortices in the far wake of the stationary cylinder dissipate faster for higher CFL numbers. This is evident from the more diffused vorticity contours seen in Figure 3.22(a) in contrast with vortices in Figure 3.5 where the vortices are more concentrated.

In addition, Figure 3.23 presents the time-averaged velocity field in the body-fixed window for the freestream flow and moving cylinder, calculated using the higher CFL = 0.6. Different from Figure 3.6, which is the same calculation performed at a lower CFL = 0.06, the wake in the

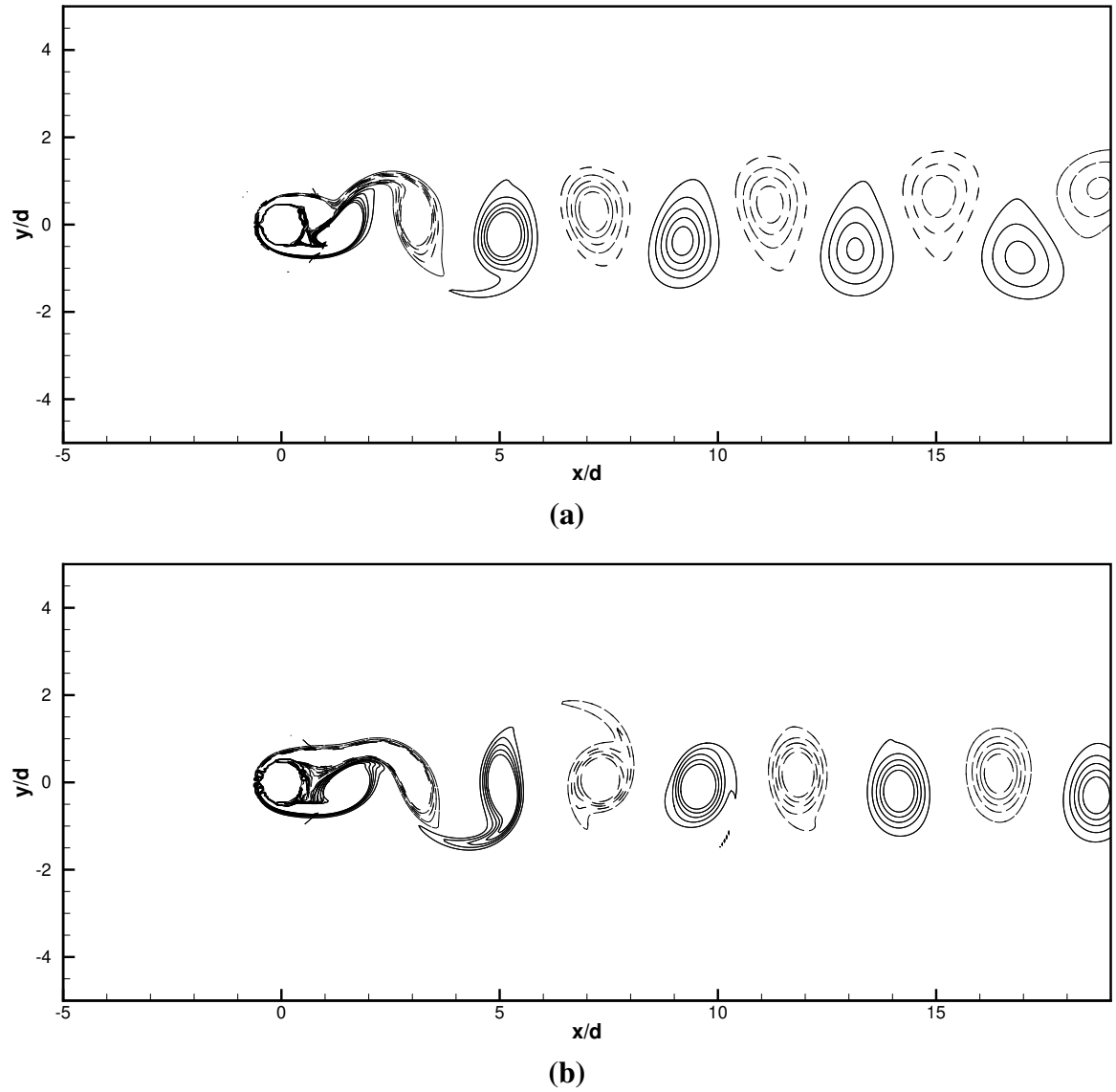

Figure 3.22: Calculated von Kármán vortex street at $Re = 400$ for (a) freestream flow and (b) moving body at quasi-steady flow time $\tau = 72$ with CFL number 0.6.

moving body simulation here is narrower and shows a smaller deficit than the freestream flow simulation.

Table 3.9 summarizes the values of $\overline{c_d}$ and St calculated in both reference frames for the different CFL numbers. While the drag coefficients calculated for the stationary cylinder display a negligible difference of 3.5%, the drag coefficients calculated for the moving cylinder decreased by 17.6% when the CFL number was increased. In addition, while the Strouhal

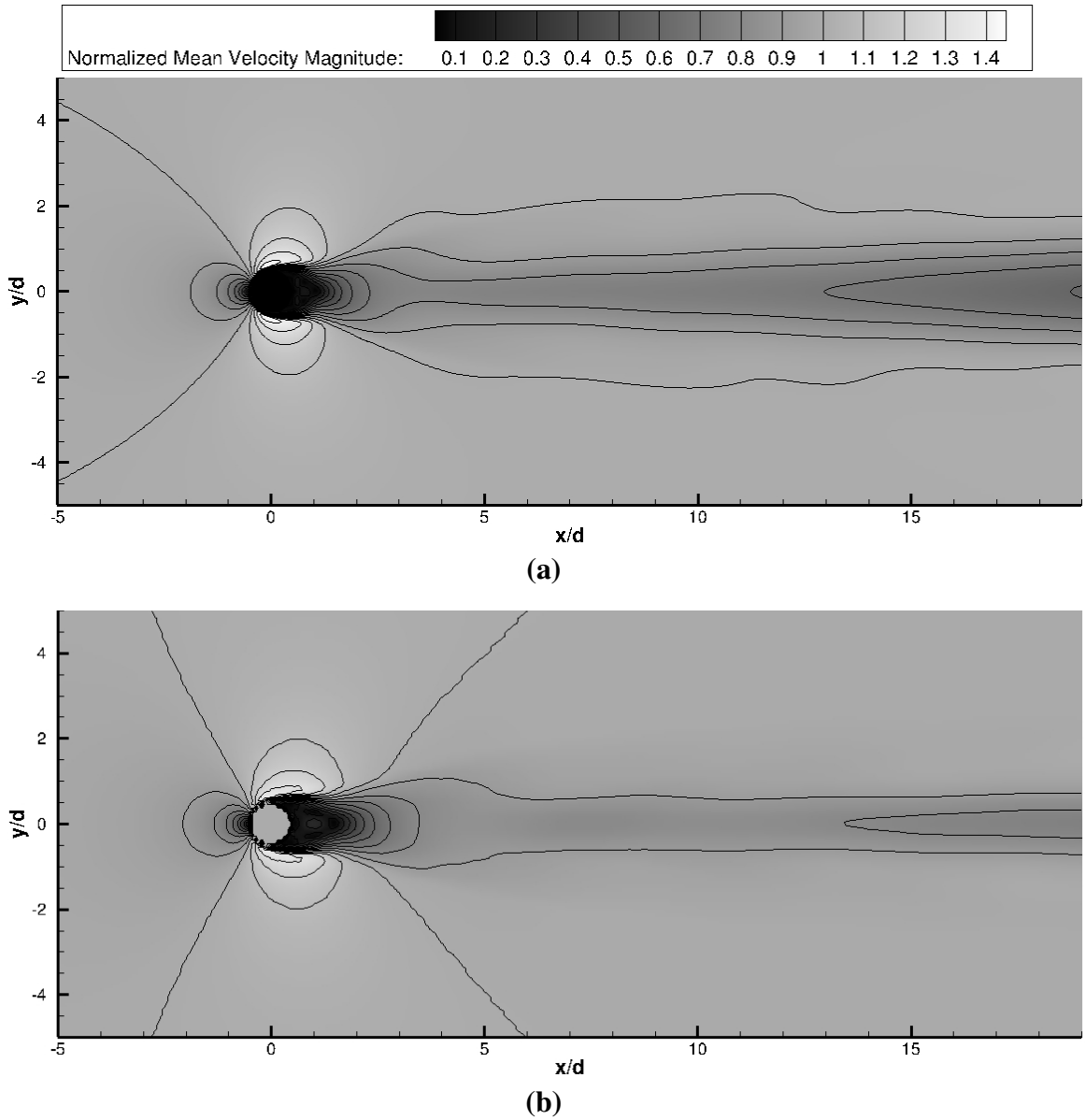

Figure 3.23: Time-averaged velocity fields for $Re = 400$ (a) freestream flow and (b) moving body simulations calculated with CFL = 0.6.

Table 3.9: Values of $\overline{c_d}$ and St calculated using different CFL numbers

	CFL=0.06	CFL=0.6	%difference
Freestream flow $\overline{c_d}$	1.4444	1.3932	3.5447
Freestream flow St	0.2083	0.2081	0.0960
Moving body $\overline{c_d}$	1.3667	1.1271	17.5313
Moving body St	0.2083	0.1943	6.7211

number calculated for the stationary cylinder case is effectively the same regardless of CFL number, the Strouhal number calculated for the moving body case decreased by 6.7% when the CFL number was increased.

Clearly, the above comparison shows that the simulations are extremely sensitive to the timestep size. This also follows the observations of Mittal and Kumar [29], who observed that secondary vortex strengths decrease significantly with decreasing timestep size. This suggests that there are multiple timescales to be resolved in this problem. For instance, the motion timescales of the cylinder are different from the timescales of the wake vortices. Hence, the CFL number must be selected very carefully regardless of what scheme is used such that both timescales can be resolved adequately. The CFL number choice may influence the accuracy of the overset interpolation for the moving body. An inappropriate timestep choice will likely result in a large amount of mesh interpolation errors if the overset patch moves across too many or too few background cells per timestep.

3.6.5 Invariance of Reference Frames

In classical physics, the common example used to illustrate invariant reference frames is that of a moving train: If the train is moving at a linear velocity, then a stationary background-fixed reference frame will be invariant to a reference frame fixed with the train's motion. However, in this example, the point of reference is the train, which can easily be approximated by a simple point mass. In contrast, fluid dynamics analysis is most concerned with the continuum of surrounding fluid in the reference frame.

Meanwhile, as described in Section 2.4, the boundary conditions used in the current simulations were chosen to resemble physical wind tunnel and atmospheric flying reference frames. In the wind tunnel, flow is driven across a test section containing a stationary body by a pressure gradient, while air is stationary in the atmosphere with no pressure gradient. Hence, a further review of the simulations' frame invariance is warranted.

It is useful to begin with the principle of material frame-indifference (MFI), which states that

only frame-indifferent terms should be present in constitutive equations [50]. MFI principle was first introduced by Truesdell and Noll [51], and is a broad axiom used to derive constitutive equations to predict the behavior of continuum materials. Speziale [52] suggested that while the MFI principle is a great approximation for most simple continuums where there is a separation of scales, the MFI principle fails when scales of motion are not cleanly separable, such as in 3D turbulence. This is the same conclusion of Lumley [53, 54] who emphasized that in a spectrum of timescales within a flow, there will always be some that lie within the timescale range of an underlying non-inertial reference frame (i.e., non-frame-invariant timescales). Additionally, Sadiki and Hutter [55] stated that form- and frame-invariance must be examined separately. Form-invariance is when observers in different reference frame apply constitutive equations in the same structure, while frame-invariance applies when the constitutive equations do not depend on any properties of the reference frames (such as boundary conditions). They claimed further that while equations can be written in a form-invariant manner, they can remain frame-variant, thus violating the MFI principle [56].

A review of the literature seems to suggest that the two frames used in this study, one with zero pressure atmospheric boundary conditions and the other with freestream flow in a wind tunnel, may not necessarily be invariant. Despite the Galilean-invariance of the Navier-Stokes equations, the different boundary conditions defining the reference frames may result in different timescales in the wake, as illustrated by the change in results when CFL number is varied, and therefore the reference frames are not inertial. However, in order to verify this, experimental validation is needed in a future study.

Chapter 4 Conclusion & Future Work

4.1 Conclusion

The preceding sections demonstrate that the wake and drag predicted for a steady laminar flow over a bluff body were largely the same when the body, fixed in place, was subjected to freestream flow, and when the same body was translating along linearly in a quiescent background fluid. However, in an unsteady laminar flow regime with vortex shedding, differences in the wake profiles and drag coefficient were obtained between both frames of reference, with the drag coefficient in the stationary cylinder case being approximately 5.69% higher. The explanation proposed is that the difference is due to the way the fluid flow was driven in both reference frames: In the case of freestream flow, the flow was driven by a pressure gradient, whereas for the case of the cylinder translating in a quiescent background fluid, the motion of the body and therefore the wake was self-induced. The boundary conditions imposed on both frames of reference in the calculation were chosen to mimic real-world scenarios, and the differences in the results imply that the scenarios may possibly be not frame-invariant. This challenges the Galilean invariance assumption for fluid dynamics simulations.

Additionally, it was also found that the motion of a bluff body in a quiescent fluid has different timescales from the wake it produced, both of which need to be resolved appropriately in order to ensure accuracy, possibly by reducing the timestep used and employing central differencing.

4.2 Future Work

To confirm that the results and conclusions presented herein are sound, experimental validation will be required. It is recommended that cylinders be towed through a long flume of water and their wakes observed via flow visualization; the same cylinder should then be fixed in place in the same flume and subject to a freestream flow, where the wakes should be likewise examined via flow visualization and compared with the first experiment. Force measurements should also

be done for both cases to estimate the drag over the cylinder.

The current results have also only covered the steady and unsteady laminar regimes with no turbulence generated. However, it is expected that the presence of turbulence at higher Reynolds numbers will have further implications on frame invariance. For example, in a wind tunnel, turbulence is prescribed and estimated at the inlet, while in flight, turbulence is self-generated by the motion of an aircraft through quiescent fluid. Additionally, due to the various scales of eddies present in turbulent flows, choosing an appropriate timestep will be even more imperative. Since prescribing turbulence at the inlet could lead to more inconsistencies in frame invariance and the simulations being very sensitive to timestep choice even in fully laminar unsteady flows, a higher Reynolds number $Re = 4000$ will be investigated using a Large-Eddy Simulation (LES). Some preliminary results are shown in Appendix D.

Finally, due to the differences between the freestream flow and moving body simulations, the development of an adaptive background mesh algorithm will be explored to enable moving body simulations without the typical high computational costs. The aim will be to remove cells far downstream of the cylinder and add cells upstream of the cylinder during runtime, or otherwise translate the background mesh boundaries together with the cylinder while preserving overset connectivity and solution continuity. This is because the moving body case is more reflective of real-world scenarios like an aircraft in cruise. Some preliminary results are shown in Appendix E and will be further developed in future.

List of References

[1] R. Mittal and S. Balachandar, "Effect of three-dimensionality on the lift and drag of nominally two-dimensional cylinders," *Physics of Fluids*, vol. 7, no. 8, pp. 1841–1865, 1995.

[2] W. D. McComb, *Dynamics and Relativity*. Oxford University Press, 1999.

[3] G. Galilei, S. Drake, and A. Einstein, *Dialogue Concerning the Two Chief World Systems, Ptolemaic and Copernican, Second Revised Edition*. University of California Press, 1953.

[4] H. D. Young, R. A. Freedman, and A. L. Ford, *University physics with modern physics*. Pearson Education, 2020.

[5] H. Oertel, *Prandtl-Essentials of Fluid Mechanics*. Springer New York, 2010.

[6] C. G. Speziale, "Galilean invariance of subgrid-scale stress models in the large-eddy simulation of turbulence," *Journal of Fluid Mechanics*, vol. 156, pp. 55–62, 1985.

[7] P. Lallemand and L.-S. Luo, "Lattice boltzmann equation with overset method for moving objects in two-dimensional flows," *Journal of Computational Physics*, vol. 407, p. 109 223, 2020.

[8] W. J. Horne and K. Mahesh, "A massively-parallel, unstructured overset method to simulate moving bodies in turbulent flows," *Journal of Computational Physics*, vol. 397, p. 108 790, 2019.

[9] A. W. Vreman, "A staggered overset grid method for resolved simulation of incompressible flow around moving spheres," *Journal of Computational Physics*, vol. 333, pp. 269–296, 2017.

[10] A. W. Vreman, "Immersed boundary and overset grid methods assessed for stokes flow due to an oscillating sphere," *Journal of Computational Physics*, vol. 423, p. 109 783, 2020.

[11] I. Gledhill, K. Forsberg, P. Eliasson, J. Baloyi, and J. Nordström, "Investigation of acceleration effects on missile aerodynamics using computational fluid dynamics,"

Aerospace Science and Technology, vol. 13, no. 4, pp. 197–203, 2009.

[12] I. M. A. Gledhill, H. Roohani, K. Forsberg, P. Eliasson, B. W. Skews, and J. Nordström, "Theoretical treatment of fluid flow for accelerating bodies," *Theoretical and Computational Fluid Dynamics*, vol. 30, no. 5, pp. 449–467, 2016.

[13] V. V. Sreedhar and A. Virmani, "Maximal kinematical invariance group of fluid dynamics and applications," *Universe*, vol. 8, no. 6, 2022.

[14] A. Y. Poludnenko and A. M. Khokhlov, "Computation of fluid flows in non-inertial contracting, expanding, and rotating reference frames," *Journal of Computational Physics*, vol. 220, no. 2, pp. 678–711, 2007.

[15] S. J. W. Joo, "Cfd simulations for bluff bodies in moving frame of reference," Nanyang Technological University, Singapore, Tech. Rep. B022, 2021.

[16] M. Mukherjee, "A numerical study of bodies in low reynolds number and their comparison in moving and stationary frames," M.S. thesis, Nanyang Technological University, Singapore, 2019.

[17] C. H. K. Williamson, "Vortex dynamics in the cylinder wake," *Annual Review of Fluid Mechanics*, vol. 28, no. 1, pp. 477–539, 1996.

[18] K. Taira, M. S. Hemati, S. L. Brunton, Y. Sun, K. Duraisamy, S. Bagheri, S. T. M. Dawson, and C.-A. Yeh, "Modal analysis of fluid flows: Applications and outlook," *AIAA Journal*, vol. 58, no. 3, pp. 998–1022, 2020.

[19] E. Anagnostopoulos and J. H. Gerrard, "A towing tank with minimal background motion," vol. 9, no. 11, pp. 951–954, Nov. 1976.

[20] J. H. Gerrard and M. J. Lighthill, "The wakes of cylindrical bluff bodies at low reynolds number," *Philosophical Transactions of the Royal Society of London. Series A, Mathematical and Physical Sciences*, vol. 288, no. 1354, pp. 351–382, 1978.

[21] M. Coutanceau and R. Bouard, "Experimental determination of the main features of the viscous flow in the wake of a circular cylinder in uniform translation. part 1. steady flow," *Journal of Fluid Mechanics*, vol. 79, no. 2, pp. 231–256, 1977.

[22] M. Coutanceau and R. Bouard, "Experimental determination of the main features of the viscous flow in the wake of a circular cylinder in uniform translation. part 2. unsteady flow," *Journal of Fluid Mechanics*, vol. 79, no. 2, pp. 257–272, 1977.

[23] D. D. Papailiou and P. S. Lykoudis, "Turbulent vortex streets and the entrainment mechanism of the turbulent wake," *Journal of Fluid Mechanics*, vol. 62, no. 1, pp. 11–31, 1974.

[24] S. Taneda, "Downstream development of the wakes behind cylinders," *Journal of the Physical Society of Japan*, vol. 14, no. 6, pp. 843–848, 1959.

[25] H. Aref and E. D. Siggia, "Evolution and breakdown of a vortex street in two dimensions," *Journal of Fluid Mechanics*, vol. 109, pp. 435–463, 1981.

[26] J. M. Cimbala, H. M. Nagib, and A. Roshko, "Large structure in the far wakes of two-dimensional bluff bodies," *Journal of Fluid Mechanics*, vol. 190, pp. 265–298, 1988.

[27] O. Inoue and T. Yamazaki, "Secondary vortex streets in two-dimensional cylinder wakes," *Fluid Dynamics Research*, vol. 25, no. 1, pp. 1–18, Jul. 1999.

[28] G. Y. Dynnikova, Y. A. Dynnikov, and S. V. Guvernyuk, "Mechanism underlying kármán vortex street breakdown preceding secondary vortex street formation," *Physics of Fluids*, vol. 28, no. 5, p. 054 101, 2016.

[29] B. Kumar and S. Mittal, "On the origin of the secondary vortex street," *Journal of Fluid Mechanics*, vol. 711, pp. 641–666, 2012.

[30] H. Jiang, "Formation mechanism of a secondary vortex street in a cylinder wake," *Journal of Fluid Mechanics*, vol. 915, A127, 2021.

[31] OpenCFD Limited, *Openfoam guide/overpimpledymfoam*, Available from `https://openfoamwiki.net/index.php/OverPimpleDyMFoam` (2022/05/23).

[32] J. Anderson, *Fundamentals of Aerodynamics* (McGraw-Hill Series in Aeronautical and). McGraw-Hill Higher Education, 2007.

[33] OpenCFD Limited, *Openfoam guide/the pimple algorithm in openfoam*, Available from `https://openfoamwiki.net/index.php/OpenFOAM_guide/The_PIMPLE_`

algorithm_in_OpenFOAM (2017/08/21).

[34] D. Triton, "Experiments on the flow past a circular cylinder at low reynolds number," *J. Fluid Mech.*, vol. 6, p. 547, 1959.

[35] O. Ilyin, "Second order accurate boundary conditions for the general propagation lattice boltzmann method," *Physics of Fluids*, vol. 33, no. 3, p. 033 110, 2021.

[36] A. Lima E Silva, A. Silveira-Neto, and J. Damasceno, "Numerical simulation of two-dimensional flows over a circular cylinder using the immersed boundary method," *Journal of Computational Physics*, vol. 189, no. 2, pp. 351–370, 2003.

[37] J. Park, K. Kwon, and H. Choi, "Numerical solutions of flow past a circular cylinder at reynolds numbers up to 160," *KSME international Journal*, vol. 12, no. 6, pp. 1200–1205, 1998.

[38] S. Dennis and G.-Z. Chang, "Numerical solutions for steady flow past a circular cylinder at reynolds numbers up to 100," *Journal of Fluid Mechanics*, vol. 42, no. 3, pp. 471–489, 1970.

[39] R. D. Henderson, "Details of the drag curve near the onset of vortex shedding," *Physics of Fluids*, vol. 7, no. 9, pp. 2102–2104, 1995.

[40] B. Rajani, A. Kandasamy, and S. Majumdar, "Numerical simulation of laminar flow past a circular cylinder," *Applied Mathematical Modelling*, vol. 33, no. 3, pp. 1228–1247, 2009.

[41] C.-Y. Wen and C.-Y. Lin, "Two-dimensional vortex shedding of a circular cylinder," *Physics of Fluids*, vol. 13, no. 3, pp. 557–560, 2001.

[42] C.-Y. Wen, C.-L. Yeh, M.-J. Wang, and C.-Y. Lin, "On the drag of two-dimensional flow about a circular cylinder," *Physics of Fluids*, vol. 16, no. 10, pp. 3828–3831, 2004.

[43] A. Roshko, "On the development of turbulent wakes from vortex streets," National Advisory Committee for Aeronautics, Washington, D.C., Tech. Rep. 1191, 1954.

[44] C. Norberg, "An experimental investigation of the flow around a circular cylinder: Influence of aspect ratio," *Journal of Fluid Mechanics*, vol. 258, pp. 287–316, 1994.

[45] H. Jiang and L. Cheng, "Transition to the secondary vortex street in the wake of a circular cylinder," *Journal of Fluid Mechanics*, vol. 867, pp. 691–722, 2019.

[46] P. Vorobieff, D. Georgiev, and M. S. Ingber, "Onset of the second wake: Dependence on the reynolds number," *Physics of Fluids*, vol. 14, no. 7, pp. L53–L56, 2002.

[47] S. Wang, "Extensions to the navier–stokes equations," *Physics of Fluids*, vol. 34, no. 5, p. 053 106, 2022.

[48] A. J. Smits and T. T. Lim, *Flow Visualization*, Second. Imperial College Press, 2012.

[49] G. E. Karniadakis and G. S. Triantafyllou, "Three-dimensional dynamics and transition to turbulence in the wake of bluff objects," *Journal of Fluid Mechanics*, vol. 238, pp. 1–30, 1992.

[50] M. Frewer, *Covariance and objectivity in mechanics and turbulence*, 2016.

[51] C. Truesdell and W. Noll, *The non-linear field theories of Mechanics*. Springer, 1992.

[52] C. G. Speziale, "A review of material frame-indifference in mechanics," *Applied Mechanics Reviews*, vol. 51, no. 8, pp. 489–504, 1998.

[53] J. L. Lumley, "Toward a turbulent constitutive relation," *Journal of Fluid Mechanics*, vol. 41, no. 2, pp. 413–434, 1970.

[54] J. L. Lumley, "Turbulence modeling," *Journal of Applied Mechanics*, vol. 50, no. 4b, pp. 1097–1103, 1983.

[55] A. Sadiki and K. Hutter, "On the frame dependence and form invariance of the transport equations for the reynolds stress tensor and the turbulent heat flux vector: Its consequences on closure models in turbulence modelling," *Continuum Mechanics and Thermodynamics*, vol. 8, no. 6, pp. 341–349, 1996.

[56] M. Frewer, "More clarity on the concept of material frame-indifference in classical continuum mechanics," *Acta Mechanica*, vol. 202, no. 1-4, pp. 247–247, 2008.

[57] P. Sagaut, *Large eddy simulation for incompressible flows*. Springer-Verlag Berlin Heidelberg, 2006.

[58] S. B. Pope and P. J. Eccles, *Turbulent Flows*. Cambridge University Press, 2000.

[59] A. G. Kravchenko and P. Moin, "Numerical studies of flow over a circular cylinder at red=3900," *Physics of Fluids*, vol. 12, no. 2, pp. 403–417, 2000.

[60] F. Nicoud and F. Ducros, "Subgrid-scale stress modelling based on the square of the velocity gradient tensor," *Flow, Turbulence and Combustion*, vol. 62, no. 3, pp. 183–200, 1999.

[61] B. Rajani, A. Kandasamy, and S. Majumdar, "Les of flow past circular cylinder at re = 3900," *Journal of Applied Fluid Mechanics*, vol. 9, no. 3, pp. 1421–1435, 2016.

[62] H. Ouvrard, B. Koobus, A. Dervieux, and M. V. Salvetti, "Classical and variational multiscale les of the flow around a circular cylinder on unstructured grids," *Computers & Fluids*, vol. 39, no. 7, pp. 1083–1094, 2010.

[63] L. Ong and J. Wallace, "The velocity field of the turbulent very near wake of a circular cylinder," *Experiments in Fluids*, vol. 20, no. 6, pp. 441–453, 1996.

Appendix A Domain Sizing

A.1 Domain Length

It was found that, if the domain length is insufficient, the drag decays over time as the cylinder moves through the domain, which is unphysical. This is illustrated in Figure A.1. As can be seen from the dashed line, for a domain length of 200m the average drag per vortex-shedding period of the cylinder decreases over time, which should not be the case as the flow is supposed to be quasi-steady. For a domain length of 600m, shown by the solid line, the decreasing trend is much less visible and instead the average drag over one vortex-shedding period of the cylinder is mostly constant. Increasing the domain length to 1000m, shown by the dotted line, does not further reduce the decay phenomenon.

A zero-pressure Dirichlet boundary condition is imposed on the left side of the moving body simulation mesh to ensure that the cylinder can entrain (or push fluid out) of the computational domain as it moves. This is because the moving cylinder induces a non-zero pressure on the near-field and, therefore, imposing a zero-pressure boundary condition too close to the cylinder

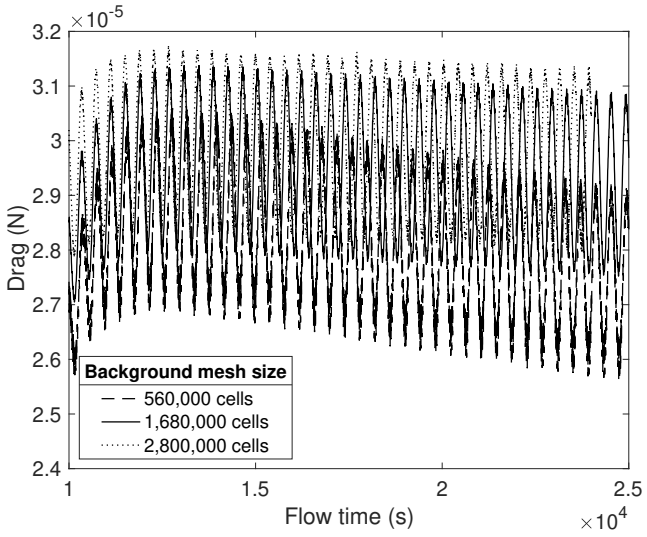

Figure A.1: Drag calculated for $Re = 400$ moving body in stationary flow using three different domain lengths, $200d$, $600d$ and $1000d$.

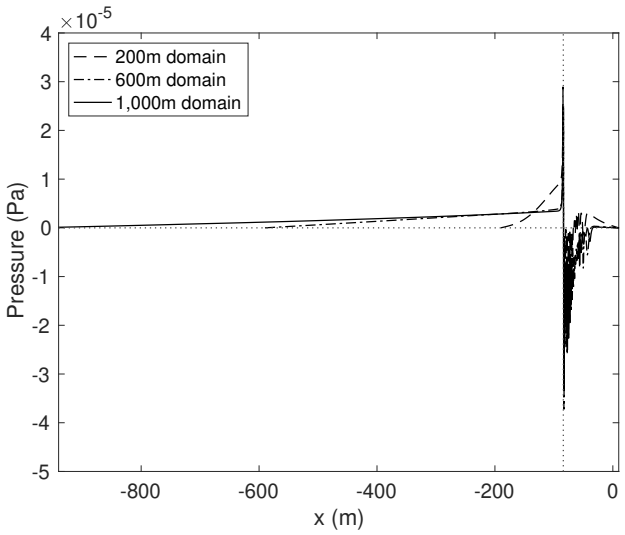

(a)

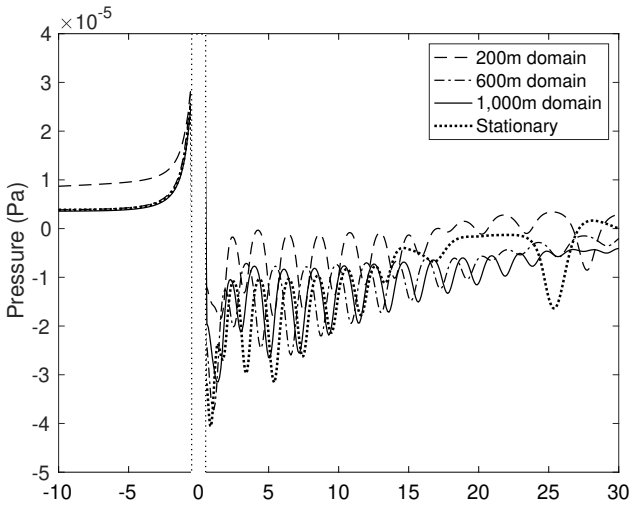

(b)

Figure A.2: Centerline pressure for $Re = 400$ probed at $t = 14000$ s for varied length of simulation domain shown (a) over entire domain and (b) in a cropped $40d$ window with origin at cylinder center.

is likely to result in inaccuracies. This problem is illustrated in Figure A.2, which shows the quasi-steady centerline pressure of the $Re = 400$ moving body simulation. As the domain length is tripled from $200d$ to $600d$ and then increased further to $1000d$, the centerline pressure upstream of the cylinder (diameter and position represented by the dashed vertical lines) approaches the centerline pressure calculated from the stationary case. The shorter domain of

$200d$ instead produces a non-zero pressure upstream (dashed line).

The plots in Figures A.1 and A.2 indicate that a domain length of 600m is most appropriate for the moving cylinder simulation. The issue with drag decay is further addressed by using a more appropriate boundary condition, as described in Appendix B.

A.2 Domain Height

The domain height needs to be sufficient to ensure that the far-field is accurately represented. Potential flow theory [32] was used to calculate the height of the potential boundary layer over the cylinder, defined by the position of zero velocity gradient. This happens approximately $5d$ from the cylinder surface. In order to account for the possibility of the wake widening, the domain top and bottom boundary was hence set at $\pm 10d$, respectively, from the center of the cylinder. It was found from simulation that the difference in drag coefficient between setting the domain top and bottom boundaries at $\pm 10d$ was negligible from setting the top and bottom boundaries at $\pm 5d$ for both stationary and moving body simulations, which is summarized in Tables A.1 and A.2 for the stationary and moving cylinders, respectively, at $Re = 400$.

Table A.1: Comparison of c_d and St values with domain height for $Re = 400$ stationary cylinder

Domain height	$\overline{c_d}$	% difference	St	%difference
$10d$	1.4250	-1.6563	0.2292	5.7683
$20d$	1.4444	-0.3175	0.2083	-3.8763
$40d$	1.4490	-	0.2167	-

Table A.2: Comparison of c_d and St values against domain height for $Re = 400$ moving cylinder

Domain height	$\overline{c_d}$	% difference	St	%difference
$10d$	1.4445	4.7954	0.2222	6.6731
$20d$	1.3667	-0.8488	0.2083	0.0000
$40d$	1.3784	-	0.2083	-

A.3 Overset Patch Sizing

Spurious numerical noise is generated in the moving body simulation if the size of the overset patch is too small. This is likely due to the propagation of inaccuracies caused by the interpolation of data from the background mesh onto the overset patch as the overset patch translates across the flow domain. The $1d$ thickness of overset patch used which consist of 3720 cells, was found to produce grid-independent result. FFT performed on the moving body simulation drag is illustrated in Figure A.3 along with the drag in the time domain, from which the noise is clearly shown by the dotted line representing an overset patch of $0.5d$. The FFT indicates that increasing the overset patch thickness beyond $1d$ produce the same frequency response, hence, the $1d$ overset patch is sufficient.

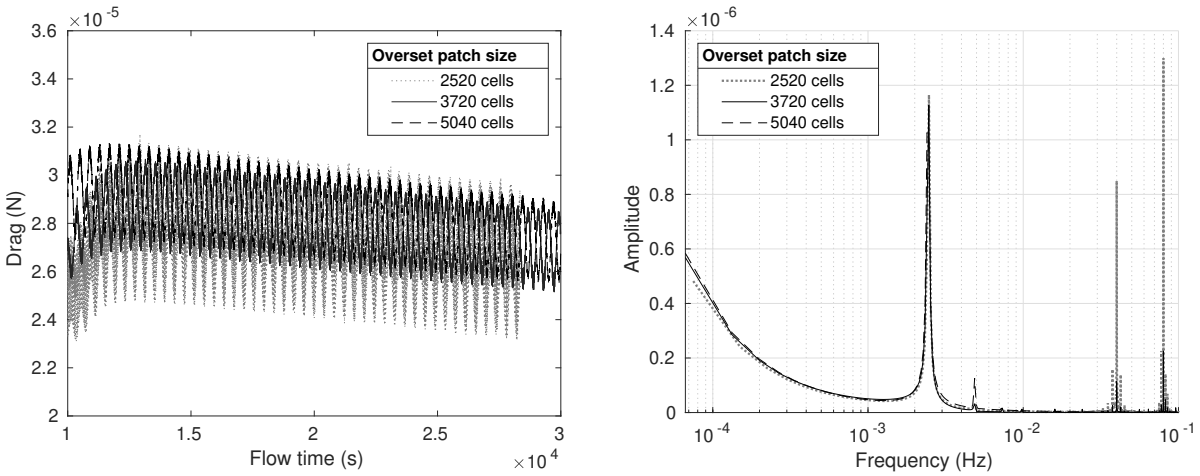

Figure A.3: Plots of drag in (a) time domain and (b) frequency domain calculated at $Re = 400$ from varied overset patch size.

Appendix B Symmetry Boundary Condition

This Appendix examines the use of the symmetry boundary condition for the moving body in quiescent fluid compared to a zero pressure boundary condition.

The boundary conditions and setup in the present study represent two real-world scenarios that are often treated as equivalent in engineering, namely: An object in motion in a quiescent fluid, for example, an aircraft in cruise, and the same object fixed in place in a wind tunnel subject to freestream flow. As such, the boundary conditions are chosen to match these two scenarios. For the case of the moving object in stationary air, the boundary conditions on all four edges of the domain were chosen to represent a still fluid, for which either $P = 0$ or $U = 0$ would ordinarily be sufficient and acceptable. However, a $U = 0$ boundary condition would be akin to enforcing no-slip on the domain walls, which is incorrect. Having this condition on the left boundary would also be unphysical, as fluid may be pushed in or out of the domain by the motion of the cylinder. Hence, $P = 0$ on all four sides was chosen instead. The velocity boundary condition was hence prescribed using the `inletOutlet` type in OpenFOAM, which sets a zero velocity gradient for outflow, and a fixed value for backflow.

Meanwhile, for the case of the stationary object in freestream flow, a pressure gradient is needed to drive the freestream flow from the inlet to the outlet. Therefore, enforcing a strict $\partial P/\partial x = 0$ boundary condition on the top and bottom edges of the domain would have been unphysical. Instead, a zero pressure gradient was set at the inlet, with the top and bottom boundaries set to freestream conditions. Likewise, the `inletOutlet` type was used for these boundaries.

Figure B.1 plots the drag against time obtained from the use of different boundary conditions, namely the symmetry boundary condition and the zero pressure boundary condition. Figure B.2 presents the corresponding vorticity contours, plotted at $t = 20000\,s$ and $t = 25000\,s$.

Using the symmetry boundary condition results in some rather unphysical stagnation points downstream of the body, as seen in Figure B.2(a), as well as a slight downward decay of the drag, as shown by the dashed line in Figure B.1. Changing the boundary conditions to zero pressure

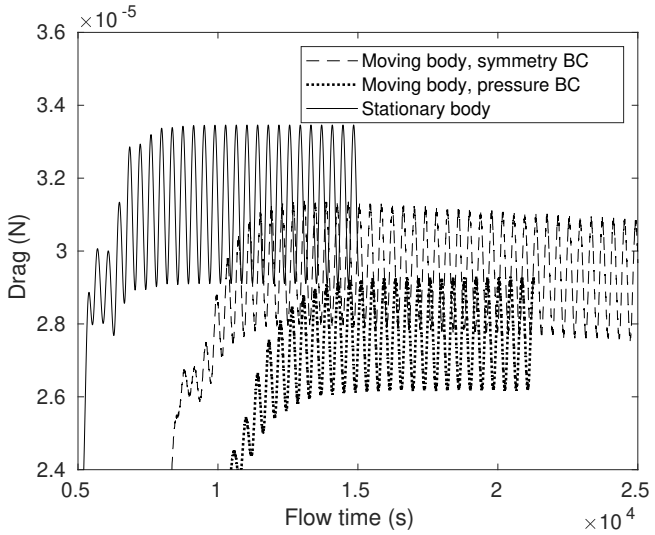

Figure B.1: Drag at $Re = 400$ calculated using different boundary condition.

instead had resolved both of these issues (Figure B.2(b) and Figure B.1 dotted line). Hence, the symmetry boundary condition was found to be unsuitable, which tallies with expectations.

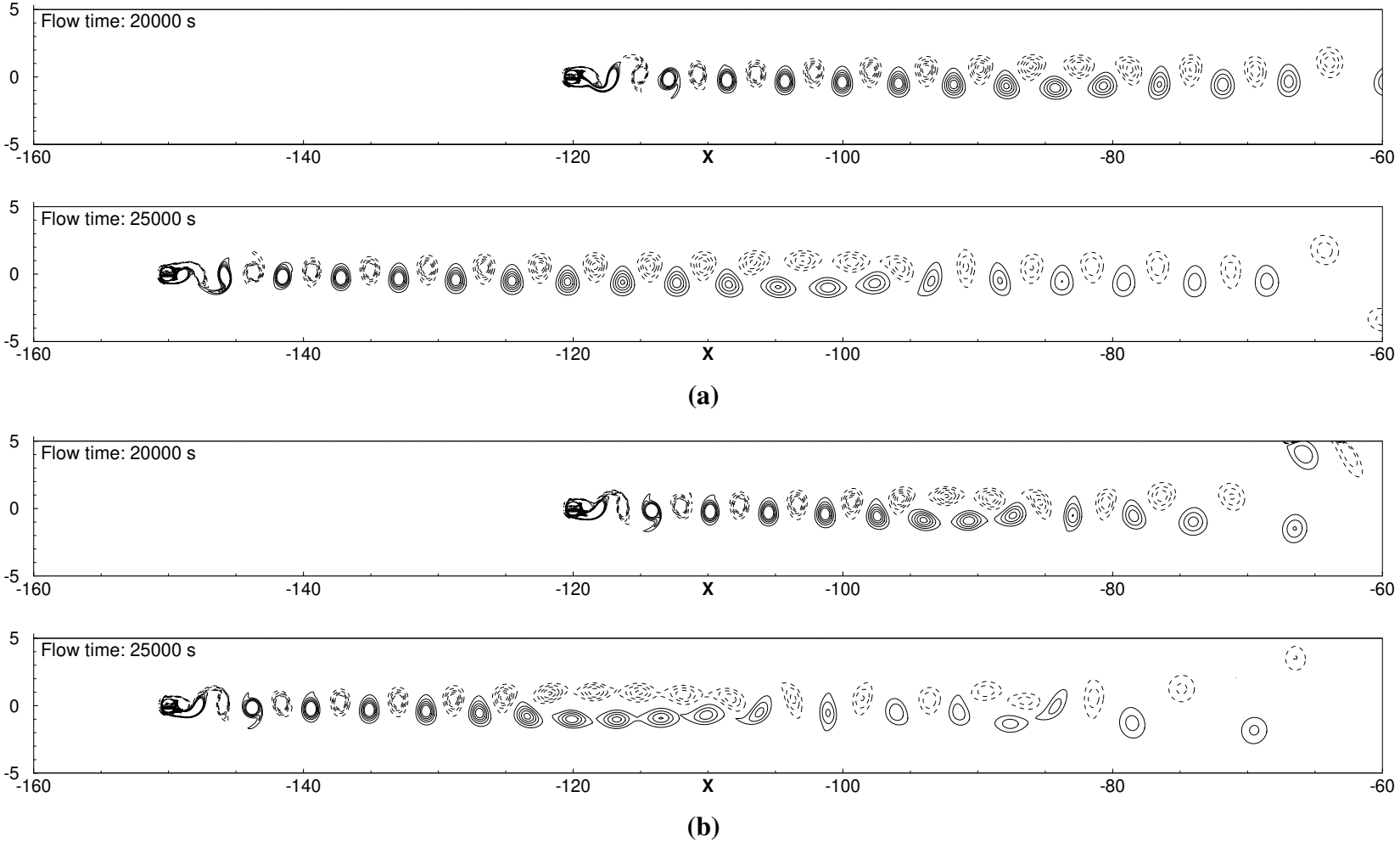

Figure B.2: Vorticity contour plots for $Re = 400$ moving body in quiescent flow calculated with different boundary condition at two different timesteps. (a) Stagnation points at the edge of the domain can be seen in the far-field of the wake for the symmetry boundary condition. (b) The zero pressure boundary condition does not produce stagnation points at the domain edges and the vorticity dissipates as the cylinder propagates.

Appendix C Comparison with ANSYS Fluent

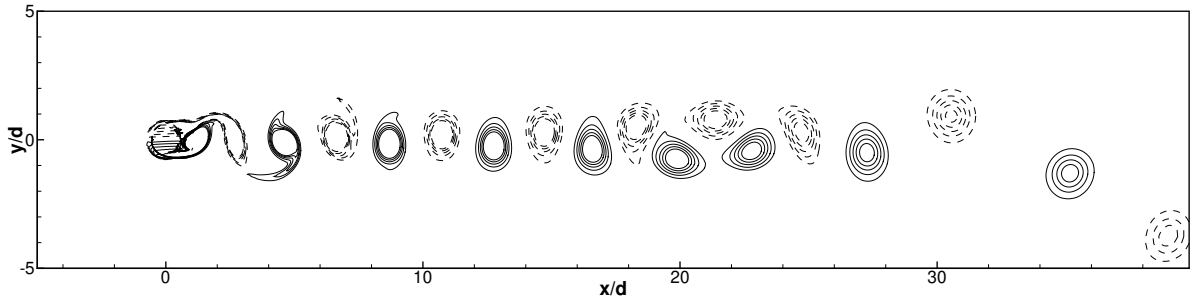

(a)

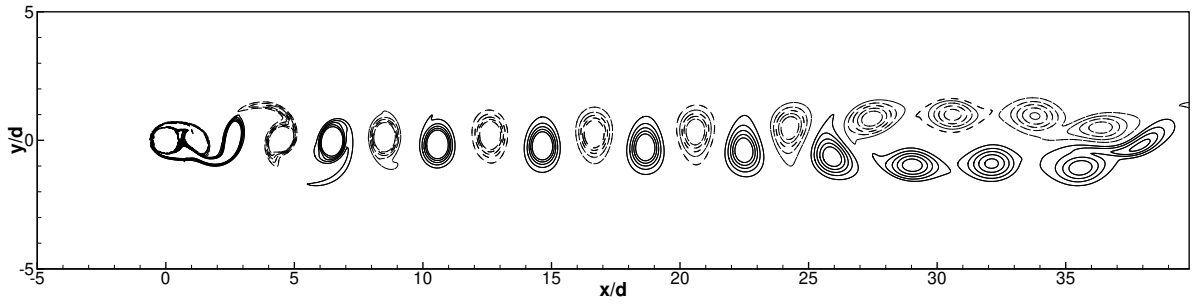

(b)

Figure C.1: Vorticity contours of moving body in quiescent flow for $Re = 400$ at $\tau = 96$ calculated by (a) ANSYS Fluent and (b) OpenFOAM.

Repeating both the stationary and moving cylinder cases with ANSYS Fluent yielded good agreement with the difference in calculated drag being less than 3% for both reference frames. The amplitude of oscillation was within 5% difference for the stationary cylinder simulation and within 4% difference for the moving cylinder simulation. The values from calculation for $Re = 400$ are summarized in Table C.1. It is suspected that the minor discrepancies are due to the difference in overset implementations between Fluent and OpenFOAM. Nevertheless, both OpenFOAM and Fluent were able to capture the same salient features of the wake flow for this simulation. This is illustrated in Figure C.1 which shows the vorticity contour plots for the moving body calculated using both solvers.

While the transition region and secondary vortex street is clearly seen in the OpenFOAM

Table C.1: $\overline{c_d}$ and St calculated for $Re = 400$ by ANSYS Fluent and OpenFOAM

	Software	**Avg.** c_d	**%change**	**Strouhal number**	**%change**
Moving cylinder	ANSYS Fluent	1.3631	2.7469	0.2083	3.8763
	OpenFOAM	1.4016		0.2167	
Stationary cylinder	ANSYS Fluent	1.3942	2.4353	0.1974	5.2328
	OpenFOAM	1.4290		0.2170	

simulation in Figure C.1(b) between $25 < x/d < 35$ with 3 pairs of vortices, the ANSYS Fluent simulation in Figure C.1(a) displays a much smaller transition region between $20 < x/d < 25$ with only two pairs of vortices. The ANSYS Fluent simulation evidently takes a longer time to reach the quasi-steady state and form the secondary vortex street.

Additionally, it should be noted that the results presented in Table C.1 were obtained using an upwind discretization scheme. This could have contributed to the minor discrepancies between the results from ANSYS Fluent and the results from OpenFOAM.

Appendix D Large-Eddy Simulation

The current results have only covered the steady and unsteady laminar regimes with no turbulence generated. However, it is expected that the presence of turbulence at higher Reynolds numbers will have further implications on frame invariance. For example, in a wind tunnel, turbulence is prescribed and estimated at the inlet, while in flight, turbulence is self-generated by the motion of an aircraft through quiescent fluid. Additionally, due to the various scales of eddies present in turbulent flows, choosing an appropriate timestep will be even more imperative. Since prescribing turbulence at the inlet could lead to more inconsistencies in frame invariance and the simulations being very sensitive to timestep choice even in fully laminar unsteady flows, a higher Reynolds number $Re = 4000$ was investigated using a Large-Eddy Simulation (LES).

D.1 Case Setup and Mesh

LES fully resolves the large scale eddies while applying averaging in space for the smaller sub-grid-scale eddies [57]. Essentially, it is a spatial filter that models the smaller eddies while computing only the larger energy-carrying eddies [58]. Hence, to obtain reasonably accurate results from LES, a finer mesh than the one presented in Chapter 2 needs to be used. Keeping the same mesh structure as described in Chapter 2 and shown in Figure 2.2, the uniform grid spacing Δx was reduced to $0.035714d$. This chosen grid spacing was based on OpenFOAM's `vortexShed` tutorial. Additionally, the number of inflation layers for the body-fitted overset patch was increased to 50 inflation layers using growth rate 1.1 and initial thickness of $0.0007d$.

The LES was done in 3D because 3D effects are expected to be significant for a turbulent cylinder wake at this Reynolds number [17]. In the $z-$axis 24 layers of cells was used and the total thickness of the domain was $\pi d/2$ following exactly Case 3 of Kravchenko & Moin [59]. Periodic boundary conditions were applied along the $z-$axis; therefore, the cylinder is essentially of infinite spanwise length.

To reduce computational costs, the domain height was reduced to $\pm 7.5d$. From the potential layer plot in Figure 2.3, this domain height should still be sufficiently far away from the cylinder and wake. The domain length in the freestream flow case was reduced to $15d$ and for the moving cylinder simulation, $400d$. Finally, the CFL number was increased to 0.28 and a blended Linear-Upwind Stabilized Transport scheme was used for convective terms in place of the purely linear scheme used in the laminar simulations.

Regarding turbulence modelling, the only model that is compatible with the overset mesh is the Wall-Adapting Local Eddy-viscosity (WALE) model, so the WALE model with standard coefficients [60] was used.

D.2 Validation

Table D.1 summarizes the mean drag coefficients and Strouhal numbers from the current stationary cylinder LES, as well as similar results from previous literature. The current 3D LES simulation compares well with the literature with the obtained drag coefficient and Strouhal number falling well within the range of previous values.

Visual inspection of the near-wake of the cylinder subject to freestream flow and comparison with Kravchenko and Moin's [59] results is shown in Figure D.1. In the current simulation, the instantaneous vorticity is averaged spanwise across the $z-$axis. Shear layer separation is clearly visible in both, and the size of the recirculation bubble just behind the cylinder is also similar.

Table D.1: Tabulated values of mean $\overline{c_d}$ and St, for $Re = 4000$.

	Type	$\overline{c_d}$	St
Kravchenko and Moin [59]	3D LES	1.04 - 1.07	0.206 - 0.212
Rajani et al. [61]	3D LES	1.01 - 1.15	0.195 - 0.214
Ouvrard et al. [62]	3D LES	0.94 - 1.16	0.212 - 0.224
Ong and Wallace [63]	Experiment		0.210
Norberg [44]	Experiment		0.210
Present work	**3D LES**	**1.0301**	**0.213**

(a)

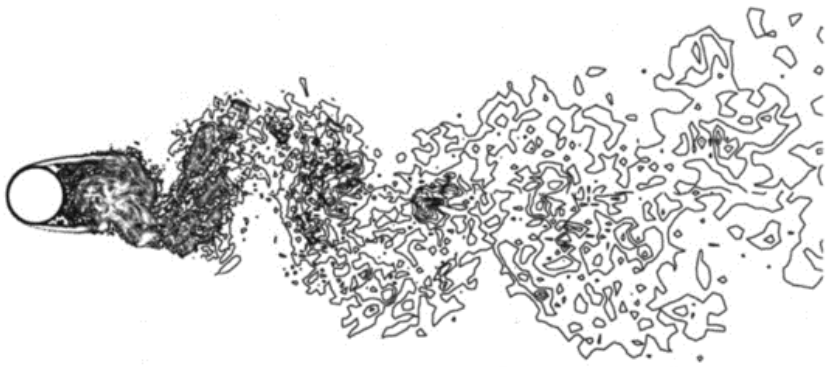

(b)

Figure D.1: Visual comparison for near-wake of $Re = 4000$ cylinder in freestream flow between (a) current simulation and (b) Kravchenko and Moin [59]. 16 contours of instantaneous vorticity are plotted between $0.5 < \omega d/U_\infty < 10$ for both figures.

D.3 Results

The mean drag coefficients for the freestream flow and moving cylinder simulations are $\overline{c_d} = 1.03$ and 1.32, respectively, representing a difference of approximately 21.74%, which is significant. This possibly indicates an insufficiently low CFL number was used and/or that the small-scale turbulence is not fully resolved in the moving cylinder simulation. Additionally the Strouhal number of $St = 0.1666$ calculated for the moving cylinder simulation also seems to be a gross underprediction compared to the literature summarized in Table D.1.

Figure D.2 shows instantaneous, span-averaged vorticity contours for the freestream flow and moving body at quasi-steady flow time $\tau = 100$, when the turbulent flow has fully developed,

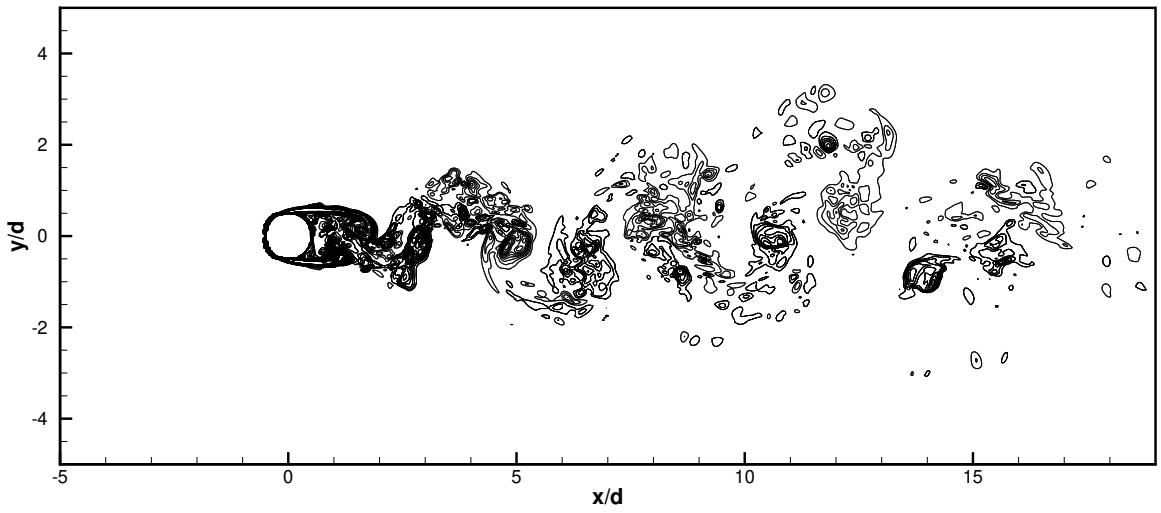

(a)

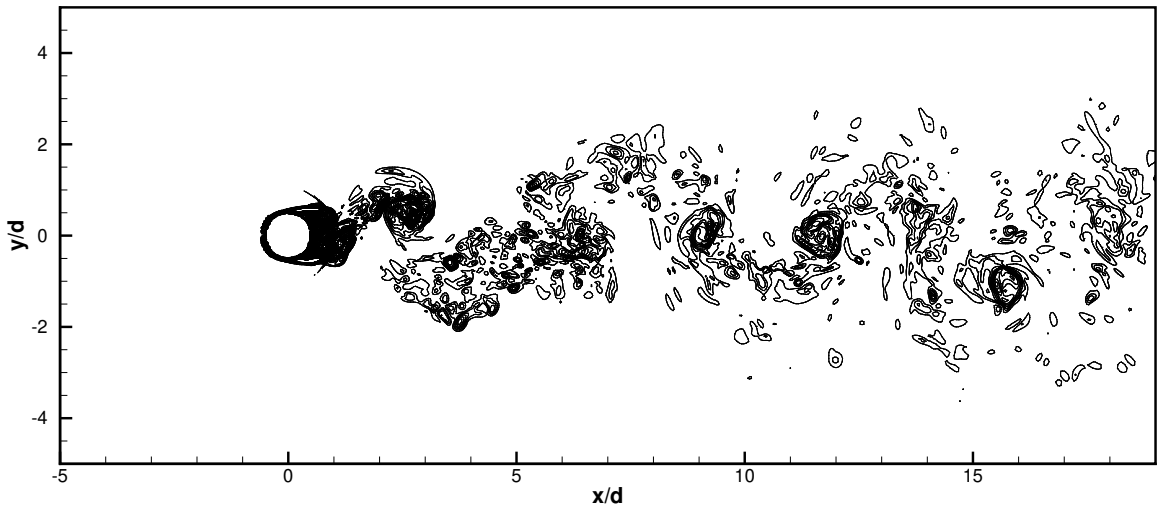

(b)

Figure D.2: Comparison of vortex-shedding for $Re = 4000$ between (a) freestream flow and (b) moving body at quasi-steady flow time $\tau = 100$.

as indicated by the steady oscillation of lift. Visually, the shear layers and recirculation region behind the cylinder is significantly smaller for the case of the moving cylinder compared to the case of the freestream flow. This discrepancy is likely the cause of the difference in drag and Strouhal number, and the size of the recirculation region and shear layers formed over the cylinder also greatly affect the downstream development of the flow [59].

It is hypothesized that the difference in the results is due to an inappropriately-sized overset

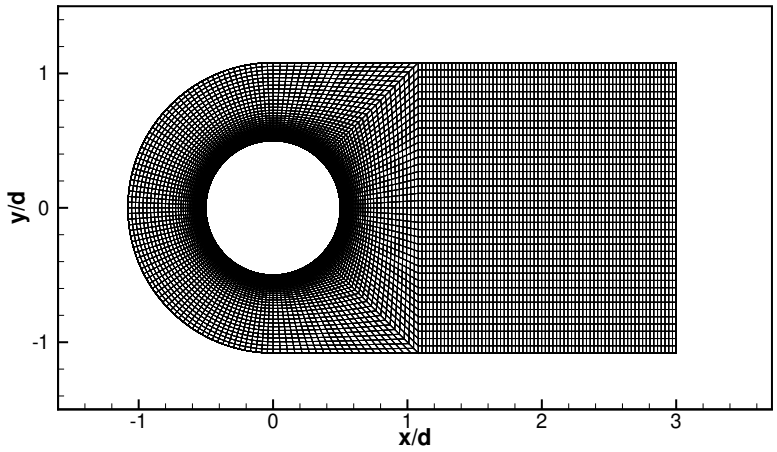

Figure D.3: Body-fitted C-type overset grid used for LES.

component. Therefore, both simulations were re-run with a C-type overset grid as shown in Figure D.3. The number of inflation layers used was kept at 50, with the same growth rate of 1.1 and initial thickness of $0.0007d$. Using this overset grid, the mean drag coefficients for the stationary and moving cylinder simulations are $\overline{c_d}$ = 1.11 and 1.09, respectively, representing a difference of approximately 1.83%, which is minimal and insignificant. However, the Strouhal number for the stationary and moving cylinder simulations were found to be $St = 0.218$ and 0.205, respectively, representing a larger difference of 6.34%. The results in both simulations were found to match well with the validation data presented in Table D.1, notably the results of Ouvrard et al. [62] who had used the same WALE turbulence model.

Instantaneous span-averaged vorticity contours from the C-type overset grid simulation at quasi-steady flow time $\tau = 100$ are presented in Figure D.4 for the stationary and moving cylinder cases. From Figure D.4 it can be seen that the recirculation region in both reference frames is of a similar size ($\simeq 2.2d$ in length). As a result, the calculated drag coefficient and Strouhal numbers are similar as well.

It should be noted, though, that all the results presented in this section have not yet reached the statistically-stationary state. Rather, these are intermediate results that were processed after the lift has reached a quasi-steady oscillation (with varying maxima). This is because the computational time required is too high, as the LES must be done in 3D. Specifically, for

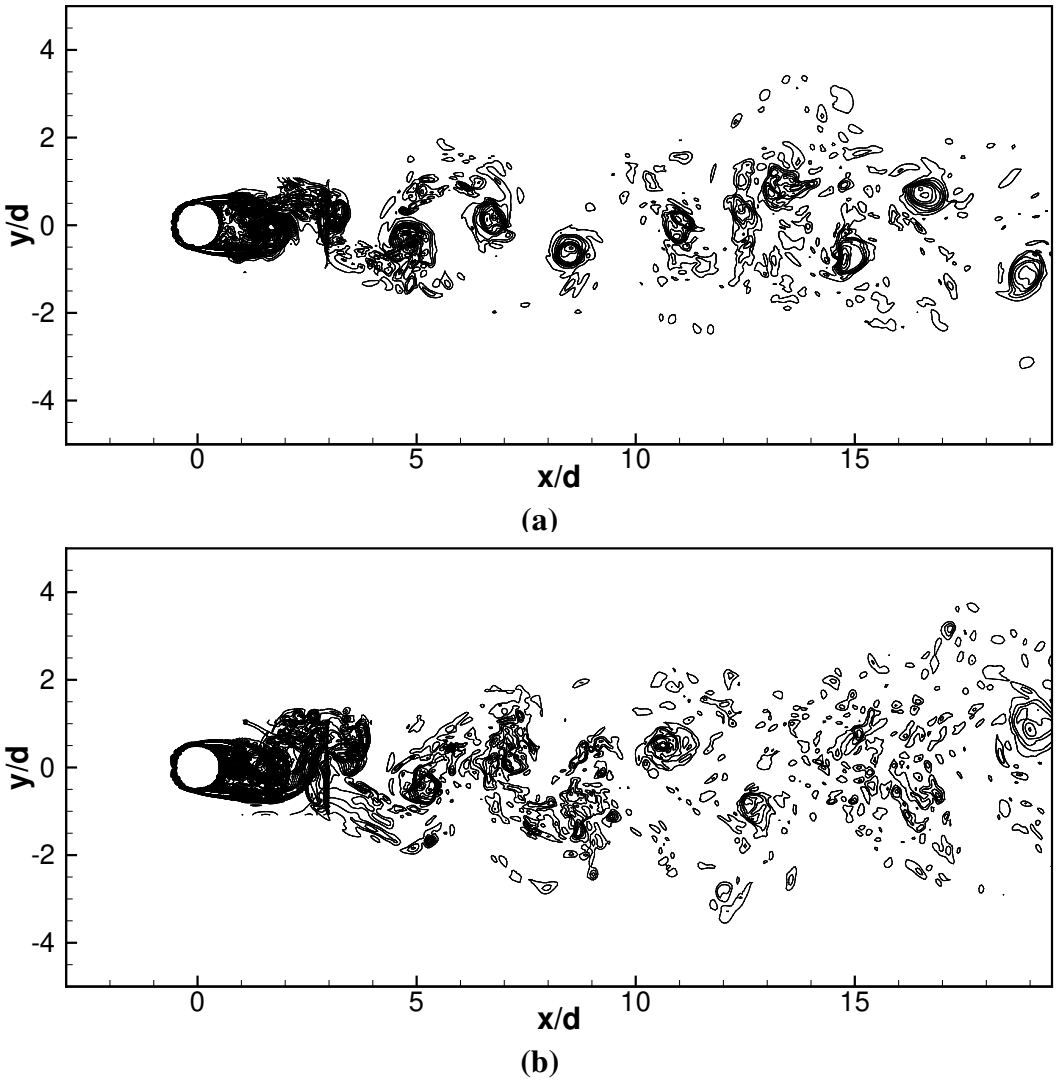

Figure D.4: Comparison of vortex-shedding for $Re = 4000$ between (a) freestream flow and (b) moving body at quasi-steady flow time $\tau = 100$ using C-type overset grid.

the moving cylinder simulation, 22 nodes on the National Supercomputing Center's ASPIRE1 cluster, each with 24 Intel Xeon E5-2690 v3 cores and 128 GB of RAM, were used to run the simulation for a total of 240 hours to reach a state where lift oscillated in a quasi-steady manner. In future work, the LES simulation will be run for a longer time. Span-averaged LES data will be processed in a similar manner to the data shown in Chapter 3. Additionally, turbulence statistics, including power spectra, will also be calculated. Finally, a frequency domain analysis as well as dynamic mode decomposition will be carried out once the LES has reached a statistically-stationary state.

Appendix E Adaptive Background Mesh

Due to the differences between the freestream flow and moving body simulations, the development of an adaptive background mesh algorithm was explored to enable moving body simulations without the typical high computational costs. The aim is to remove cells far downstream of the cylinder and add cells upstream of the cylinder during runtime, or otherwise translate the background mesh boundaries together with the cylinder while preserving overset connectivity and solution continuity.

The proposed algorithm is as follows, corresponding to the schematic shown in Figure E.1:

1. Pause simulation at n timesteps
2. Translate cloned copy of background mesh by distance $x = n\Delta t$
3. Clone translated background mesh
4. Add overset patch to translated background mesh
5. Interpolate data from paused simulation
6. Re-initialize overset connectivity
7. Continue simulation

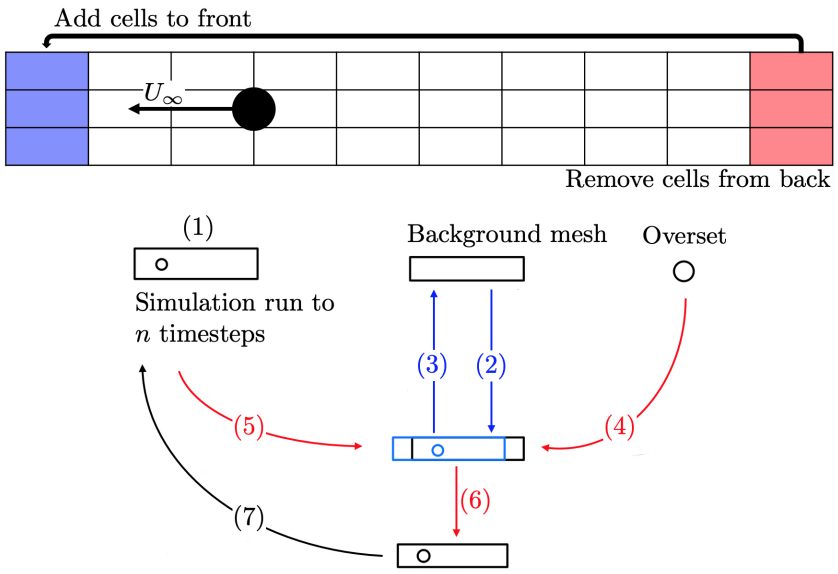

Figure E.1: Schematic of background remeshing algorithm.

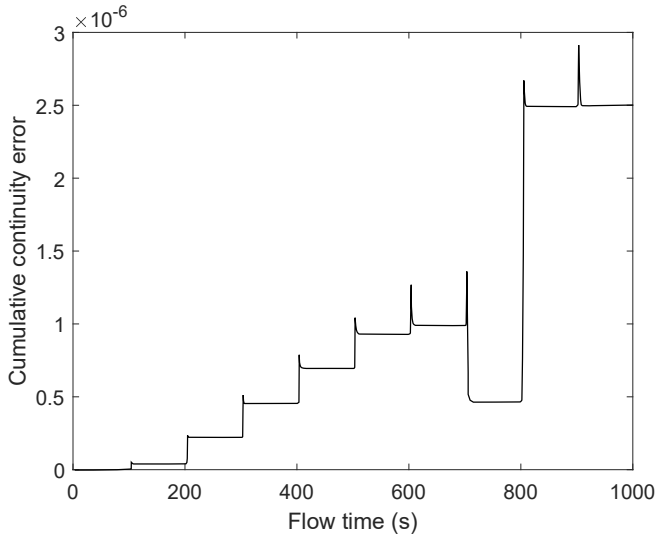

Figure E.2: Cumulative continuity error of $Re = 400$ simulation with background remeshing for 1000 timesteps.

While the algorithm was able to run, the obtained results displayed large amounts of continuity error that accumulated after every translation/interpolation. This is illustrated in Figure E.2, which shows the cumulative continuity error from running the $Re = 400$ cylinder simulation with the background remeshing algorithm run every $n = 200$ timesteps ($\Delta t = 0.5$s).

Further investigation was done by coarsening the mesh and changing the cylinder to a square. Pressure contours are illustrated in Figure E.3, which shows that an error is introduced on the overset patch (shown by the white edges) after interpolation, as the data before and after the interpolation is different. This is likely due to a lack of two-way coupling between the overset and the background during the simulation. Hence, while the overset data is interpolated to the background mesh during the course of the simulation, the reverse is not true [31]. This necessitates Step 5 in Figure E.1, but data on the overset mesh is flushed when the overset connectivity is re-initialized.

To resolve this issue, two possibilities would be either modifying existing OpenFOAM adaptive meshing codes, such as `movingConeTopoFvMesh`, or modifying the overset code such that data is re-interpolated to the overset patch after re-initializing the overset connectivity. Regarding the pre-existing adaptive meshing codes, all the pre-existing utilities require a reference patch

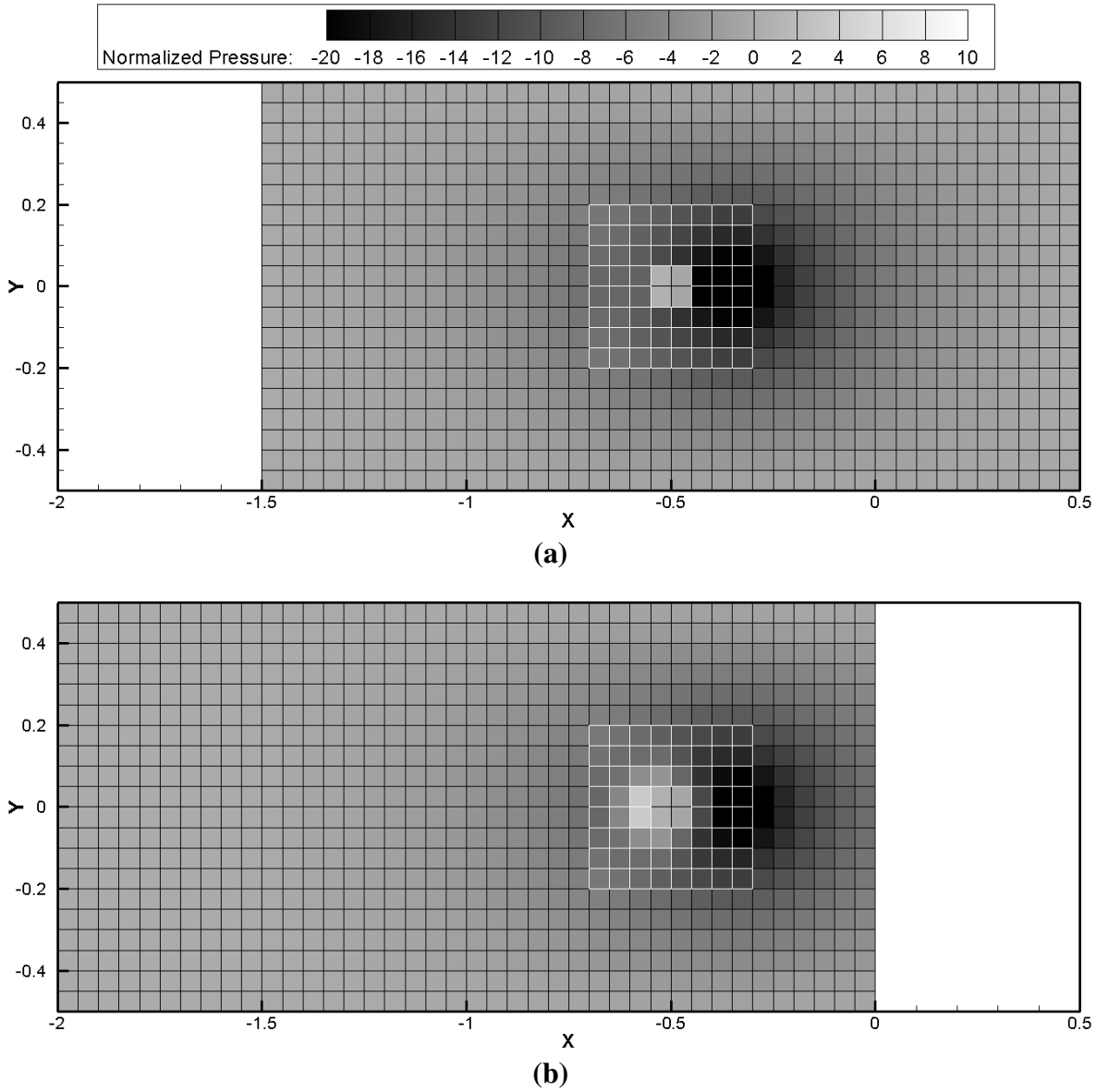

Figure E.3: Pressure contours of square (a) before and (b) after background remeshing.

in order to remesh dynamically. Therefore, likely a sliding interface is required to suit the current case setup.